Study of the Effective Young's Modulus of Carbon Nanotube-Based Polymer Composites Using Finite Element Method

by

Abdullah-Al-Khaled

A Thesis

Submitted As the Partial Fulfillment for the Degree Of

MASTER OF SCIENCE IN INDUSTRIAL & PRODUCTION ENGINEERING

DEPARTMENT OF INDUSTRIAL & PRODUCTION ENGINEERING

BANGLADESH UNIVERSITY OF ENGINEERING AND TECHNOLOGY

Dhaka-1000, Bangladesh

April 2008

The thesis titled **"Study of the Effective Young's Modulus of Carbon Nanotube-Based Polymer Composites Using Finite Element Method"** submitted by **Abdullah-Al-Khaled, Roll No: 100508004P** has been accepted as satisfactory in partial fulfillment of the requirement for the degree of Master of science in Industrial & Production Engineering on 05/04/08

BOARD OF EXAMINERS

1. ______________________ Chairman (Supervisor)

Dr. A.K.M. Masud
Associate Professor
Department of Industrial & Production Engineering
Bangladesh University of Engineering & Technology (BUET)
Dhaka, Bangladesh

2. ______________________ Member (Co-Supervisor)

Dr. Sanjib Chandra Chowdhury
Assistant Professor
Department of Mechanical Engineering, BUET, Dhaka, Bangladesh

3. ______________________ Member

Dr. Nikhil Ranjan Dhar
Professor
Department of Industrial & Production Engineering, BUET, Dhaka, Bangladesh

4. ______________________ Member

Dr. Abdullahil Azeem
Assistant Professor
Department of Industrial & Prodnction Engineering, BUET, Dhaka, Bangladesh

5. ______________________ Member (Ex-officio)

Dr. Md. Ahsan Akhtar Hasin
Professor and Head
Department of Industrial & Production Engineering, BUET, Dhaka, Bangladesh

6. ______________________ Member (External)

Dr. Md. Fakhrul Islam
Professor and Head
Department of Materials & Metallurgical Engineering, BUET, Dhaka, Bangladesh

CANDIDATE'S DECLATION

It is hereby declared that this thesis or any part of it has not been submitted elsewhere for the award of any degree or diploma.

Khaled

Abdullah-Al-Khaled

CONTENTS

Title	Page
CANDIDATE'S DECLARATION	iii
CONTENTS	iv
LIST OF FIGURES	vii
LIST OF TABLES	xi
NOMENCLATURE	xii
ACKNOWLEDGEMENT	xiii
ABSTRACT	xiv
CHAPTER 1 INTRODUCTION	**1**
1.1 Structure of Carbon Nanotubes	1
1.2 Properties of Carbon Nanotubes	5
1.3 Motivation of the Present Work	6
1.4 Objectives	7
CHAPTER 2 LITERATURE REVIEW	**9**
2.1 Summary	12
CHAPTER 3 THEORETICAL BACKGROUND	**13**
3.1 Fundamental Equations	13
3.1.1 Stress-strain relations	13
3.1.2 The equilibrium equations	15
3.2 Finite Element Method	17
3.2.1 Finite element formulation	19

3.3 Finite Element Software 30
3.3.1 General description of the software 31
3.3.2 Basic steps in the finite element method 31
3.3.3 Two dimensional axi-symmetric elements used in the software 32
3.3.4 The frontal solver 36

CHAPTER 4 COMPUTATIONAL DETAILS 38
4.1 RVEs for Evaluation of the Effective Material Property 38
4.2 Formulation of Equation Used to Determine the Effective Young's Modulus 40
4.3 Analytical Solution Based on the Strength of Materials Theory 42
4.3.1 RVE for long CNT 43
4.3.2 RVE for short CNT 44
4.4 Modeling the Problem in the Finite Element Software 45
4.4.1 Pre-processing of the models 46
4.4.2 Boundary conditions and the solution 46
4.4.3 Post processing 48

CHAPTER 5 RESULTS AND DISCUSSION 49
5.1 Effect of CNT Diameter on the TEM of Nanocomposite for Perfect Bonding 50
5.2 Effect of CNT Diameter on the TEM of Nanocomposite for Imperfect Bonding 56
5.3 Effect of Interphase Thickness on the TEM of Nanocomposite 61
5.4 Effect of CNT Wall Thickness on the TEM of Nanocomposite for Perfect Bonding 66
5.5 Effect of CNT Waviness on the TEM of Nanocomposite 71

5.6 Effect of CNT Wavelength on the TEM of Nanocomposite 75

CHAPTER 6 CONCLUSIONS **78**

6.1 Conclusions 78

6.2 Recommendations 79

REFERENCES **81**

LIST OF FIGURES

Figure 1.1	Roll-up vector defining the structure of carbon nanotubes (a) Graphene lattice and (b) Carbon nanotube	2
Figure 1.2	Different types of carbon nanotubes (a) Armchair (b) Zigzag and (c) Chiral	4
Figure 1.3	Carbon nanotubes (a) Single-walled nanotube (SWNT) (b) Multi-walled nanotube (MWNT)	5
Figure 2.1	Three nanoscale RVEs for the analysis of CNT-based composites, (a) Cylindrical (b) Square and (c) Hexagonal	12
Figure 3.1	PLANE42 element used by ANSYS 10.0	32
Figure 3.2	PLANE82 element used by ANSYS 10.0	33
Figure 3.3	PLANE83 element used by ANSYS 10.0	34
Figure 3.4	PLANE182 element used by ANSYS 10.0	35
Figure 3.5	PLANE183 element used by ANSYS 10.0	35
Figure 3.6	Typical steps and files in a frontal solution	37
Figure 4.1	The cylindrical RVE with long CNT	39
Figure 4.2	The cylindrical RVE with short CNT (cut-through view)	40
Figure 4.3	The cylindrical RVE used to evaluate the TEM of the CNT-based composites under axial stretch ΔL	41
Figure 4.4	Simplified strength of materials models used to derive analytical expressions for the effective Young's modulus, E_z (a) CNT through the length of RVE, (b) CNT inside the RVE	43
Figure 4.5	Partial view of the models after meshed (a) with long CNT; and (b) with short CNT	47

Figure 5.1	Axi-symmetric finite element mesh for the long CNT-based model with 10.85 nm of CNT diameter, (a) full view (b) partial enlarged view.	51
Figure 5.2	Plot of the first principal stresses for the long CNT-based model with 10.85 nm of CNT diameter under the axial stretch (ΔL = 1 nm)	52
Figure 5.3	Effect of nanotube diameter variation on the TEM of nanocomposite for long CNT (V_{CNT} = 5%)	53
Figure 5.4	Axi-symmetric finite element mesh for the short CNT-based model with 10.85 nm of CNT diameter, (a) full view (b) partial enlarged view.	54
Figure 5.5	Plot of the first principal stresses for the short CNT-based model with 10.85 nm of CNT diameter under the axial stretch (ΔL = 1 nm)	55
Figure 5.6	Effect of nanotube diameter variation on the TEM of nanocomposite for short CNT (VCNT = 5%)	56
Figure 5.7	Partial view of the finite element mesh of the long CNT-based model for imperfect bonding	58
Figure 5.8	Plot of the first principal stresses for the RVE (long CNT) with 0.2 nm thick interphase under axial stretch (ΔL = 1 nm)	58
Figure 5.9	Effect of nanotube diameter variation on the TEM of nanocomposite with long CNT for imperfect bonding (V_{CNT} = 5%)	59
Fignre 5.10	Partial view of the finite element mesh of the short CNT-based model for imperfect bonding.	60
Figure 5.11	Plot of the first principal stresses for the RVE (short CNT) with 0.2 nm thick interphase under axial stretch (ΔL = 1 nm)	60
Figure 5.12	Effect of nanotube diameter variation on the TEM of nanocomposite for short CNT with imperfect bonding (V_{CNT} = 5%)	61
Figure 5.13	Partial view of the finite element mesh of the long CNT-based model with 0.6 nm thick interphase	62

Figure 5.14	Plot of the first principal stresses for the RVE (long CNT) with 0.6 nm thick interphase under axial stretch (ΔL = 1 nm)	63
Figure 5.15	Effect of interphase thickness variation on the TEM of nanocomposite for long CNT (V_{CNT} = 5%)	63
Figure 5.16	Partial view of the finite element mesh of the short CNT-based model with 0.6 nm thick interphase	64
Figure 5.17	Plot of the first principal stresses for the RVE (short CNT) with 0.6 nm thick interphase under axial stretch (ΔL = 1 nm)	65
Figure 5.18	Effect of interphase thickness variation on the TEM of nanocomposite for short CNT (V_{CNT} = 5%).	65
Figure 5.19	Partial view of the finite element mesh for the long CNT-based model with 1.2 nm of CNT wall thickness	68
Figure 5.20	Plot of the first principal stresses for the RVE (long CNT) with 1.2 nm of CNT wall thickness under axial stretch (ΔL = 1 nm)	68
Figure 5.21	Partial view of the finite element mesh of the short CNT-based model with 1.2 nm of CNT wall thickness	69
Figure 5.22	Plot of the first principal stresses for the RVE (short CNT) with 1.2 nm of CNT wall thickness under axial stretch (ΔL = 1 nm)	70
Figure 5.23	Effect of CNT wall thickness variation on the TEM of nanocomposite (V_{CNT} = 5%)	70
Figure 5.24	Finite element mesh of the model with 3 nm amplitude of sinusoidal CNT for perfect bonding, (a) full view (b) partial enlarged view	72
Figure 5.25	Plot of the first principal stresses for the RVE with CNT waviness ratio of (a/λ = 0.015) for perfect bonding under axial stretch (ΔL = 1 nm).	73
Figure 5.26	Partial view of the finite element mesh with 3 nm amplitude of sinusoidal CNT for imperfect bonding.	73
Figure 5.27	Plot of the first principal stresses for the RVE with CNT waviness ratio of (a/λ = 0.015) for imperfect bonding under	74

axial stretch (ΔL = 1 nm)

Figure 5.28	Effect of waviness ratio (a/λ) variation on the TEM of nanocomposite for wavelength ratio, λ/d = 13.406 (V_{CNT} = 5%)	75
Figure 5.29	Partial view of the finite element mesh with 4 nm amplitude of sinusoidal CNT for perfect bonding	76
Figure 5.30	Plot of the first principal stresses for the RVE with CNT wavelength ratio of (λ/d = 13.406) under axial stretch (ΔL = 1 nm)	76
Figure 5.31	Effect of wavelength ratio (λ/d) variation on the TEM of nanocomposite for different values of waviness ratio (V_{CNT} = 5%)	77

LIST OF TABLES

Table 1.1	Types of nanotubes based on chiral indices	3
Table 5.1	The radii of matrix and CNT for different values of CNT diameter for long CNT-based model	50
Table 5.2	The radii of matrix for different values of CNT diameter for short CNT-based model	54
Table 5.3	The radii of matrix and CNT for different values of CNT wall thicknesses for long CNT-based model	67
Table 5.4	The radii of matrix for different values of CNT wall thicknesses for short CNT-based model	69

NOMENCLATURE

a	Amplitude of sinusoidal carbon nanotube
a/λ	Waviness ratio of sinusoidal carbon nanotube
a_1	Vector of the hexagonal graphite lattice
a_2	Vector of the hexagonal graphite lattice
a_0	Length of vectors a_1 or a_2
b	Body force vector
B	Strain-displacement matrix
C_h	Chiral vector or roll-up vector of carbon nanotube
CNT	Carbon nanotube
D	Elasticity matrix
E	Modulus of elasticity
FEM	Finite element method
G	Modulus of rigidity
K	Global stiffness matrix
MD	Molecular dynamics
r	Radial component of polar co-ordinate system
RVE	Representative volume element
R_{NT}	Radius of carbon nanotube
SWNT	Single-walled nanotube
MWNT	Multi-walled nanotube
TEM	Tensile elastic modulus
z	Axial component of polar co-ordinate system
θ	Chiral angle
v	Poisson's ratio
ε	Normal strain
γ	Shear strain
τ	Shear stress
δ	Nodal displacement matrix
σ	Normal stress

ACKNOWLEDGEMENT

The author would like to take the opportunity of expressing his heartiest gratitude to his thesis supervisor Dr. A.K.M. Masud, Associate Professor, Department of Industrial & Production Engineering, Bangladesh University of Engineering and Technology (BUET), Dhaka, Bangladesh, for his careful supervision, guidance, valuable suggestions and encouragement throughout this research work.

The author expresses heartfelt gratitude and indebtedness to his thesis co-supervisor Dr. Sanjib Chandra Chowdhury, Assistant Professor, Department of Mechanical Engineering, BUET, for his careful guidance, valuable suggestions and encouragement in completing the thesis work.

The author is grateful to Dr. Ashutosh Sutradhar, Associate Professor, Department of Civil Engineering, BUET, for his help during working with ANSYS 10.0. He is very much indebted to Md. Obayedullah, Associate Professor, Department of Mathematics, for his enormous help during the formulation of finite element method. He is also indebted to Sumon Saha, Lecturer, Department of Mechanical Engineering, BUET, for his continuous help and encouragement throughout this thesis work

The author would like to express his gratitude to Seratun Jannat, Lecturer, Department of Industrial & Production Engineering, BUET, who has assisted both directly and indirectly in the preparation of this research work. The author also wants to thank all the teachers and staffs of Industrial & Production Engineering Department, BUET, for their help and inspiration.

Finally, the author also thanks sincerely his parents, family, relatives and friends, who supported a lot for completion of this thesis work.

ABSTRACT

Carbon nanotubes (CNTs) possess extremely high stiffness, strength and resilience and may provide the ultimate reinforcing materials for the development of nanocomposites. It is found that the degree of nanotube reinforcement in polymer-based nanocomposites observed in different experiments differs significantly. In the present research work, six different aspects of CNT-based polymer composites are investigated to observe their effects on the effective tensile elastic modulus (TEM) of such nanocomposites. They are--effect of CNT diameter for both perfect and imperfect bonding, effect of interphase thickness developed between CNT and matrix, effect of CNT wall thickness, effect of CNT waviness ratio and effect of CNT wavelength ratio for different waviness ratios on the TEM of nanocomposites. These investigations are carried out for the nanocomposites containing both long and short CNTs. For all cases, volume fraction of the CNTs is considered only 5%. This effective TEM is evaluated using a 3-D nanoscale representative volume element (RVE) based on continuum mechanics and using the finite element method (FEM). The finite element modeling and analyses are carried out using the commercial software ANSYS 10.0. Due to symmetry of the RVEs about the axial axis, axi-symmetric finite element modeling and analyses are conducted to evaluate the effective TEM. Finite element formulation for the axi-symmetric model is presented in detail. Formula to extract the effective TEM from FEM solutions for the RVE is derived based on the elasticity theory. An extended rule of mixtures, based on the strength of materials theory for estimating the effective TEM in the axial direction of the RVEs, is applied for comparisons with the numerical solutions. These investigations, using the FEM, are presented in detail, which demonstrate that the load carrying capacities of the CNTs in a polymer matrix are significantly affected by the above mentioned issues. These simulation results are consistent with the available analytical and experimental results.

CHAPTER 1
INTRODUCTION

Since their first synthesis by Endo in 1976 [1] and detailed characterization by Iijima in 1991 [2], carbon nanotubes (CNTs) have grown from a material of dreams to a "real-world" material that has already found its application fields. The production capability for CNTs is growing every year in an exponential degree, and as a consequence the price is steeply descending. This is leading to the application of carbon nanotubes in various conventional and unprecedented areas, including lightweight structural composites, field emission devices, electronics, nano-electro-mechanical devices, sensors, actuators, gas storage, medical applications and nano-robotics.

1.1 STRUCTURE OF CARBON NANOTUBES

CNTs can be visualized as a sheet of graphite that has been rolled into a tube These are long, slender fullerenes where the walls of the tubes are hexagonal carbon (graphite structure) and often capped at each end. Unlike diamond, where a 3-D diamond cubic crystal structure is formed with each carbon atom having four nearest neighbors arranged in a tetrahedron, graphite is formed as a 2-D sheet of carbon atoms arranged in a hexagonal array In this case, each carbon atom has three nearest neighbors. 'Rolling' sheets of graphite into cylinders forms carbon nanotubes, shown in Fig. 1.1 [3].

The direction along which the graphite sheet is rolled up to form the nanotube determines its chirality and also affects whether the nanotube is metallic or behaves like a semiconductor. This direction of roll is defined by a vector known as 'roll-up vector' or 'chiral vector', C_h, and can be expressed as a linear combination of the unit translational vectors in the hexagonal lattice [3].

$$C_h = ma_1 + na_2 \tag{1.1}$$

Here, m and n are integers, while a_1 and a_2 are the vectors of the hexagonal graphite lattice shown in Fig. 1.1(a). The angle between C_h and a_1 is known as the chiral angle, θ, and can be calculated as follows [3]:

$$\theta = \sin^{-1}\left[\frac{\sqrt{3}m}{\sqrt{m^2+mn+n^2}}\right] \tag{1.2}$$

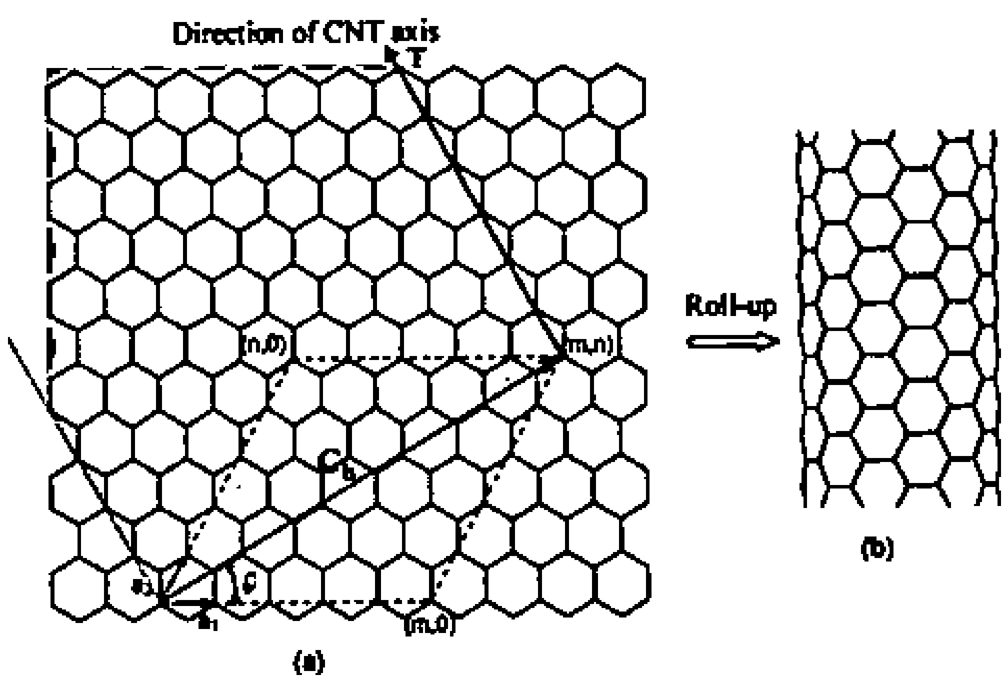

Figure 1.1: Roll-up vector defining the structure of carbon nanotubes (a) Graphene lattice and (b) Carbon nanotube

The variation of the chiral indices (m, n) and chiral angle, θ, result in different types of nanotubes. Table 1.1 summarizes three major categories of nanotubes which could be formed depending on chiral indices (m, n).

Table 1.1. Types of nanotubes based on chiral indices

Type of nanotube	**Chiral indices (m,n)**	**Chiral angle, θ**	**Tube diameter, D_{NT}**
Zigzag	$(m,0)$	0	$\frac{a_0 m}{\pi}$
Armchair	(m,m)	30°	$\frac{\sqrt{3}a_0 m}{\pi}$
Chiral	(m,n); $m \neq n \neq 0$	$0<\theta<30°$	$\frac{a_0\sqrt{(m^2+mn+n^2)}}{\pi}$

The radius of any nanotube can be calculated as follows [3]:

$$R_{NT} = \frac{a_0\sqrt{m^2+mn+n^2}}{2\pi} \tag{1.3}$$

Where, a_0 is the length (in nm) of vector a_1 (or a_2), see Fig. 1.1. Typical examples of the three types of CNTs are shown in Fig. 1.2 [3].

Again, CNTs exist as either single-walled (SWNT) or multi-walled (MWNT) structures, as shown in Fig. 1.3 [3].

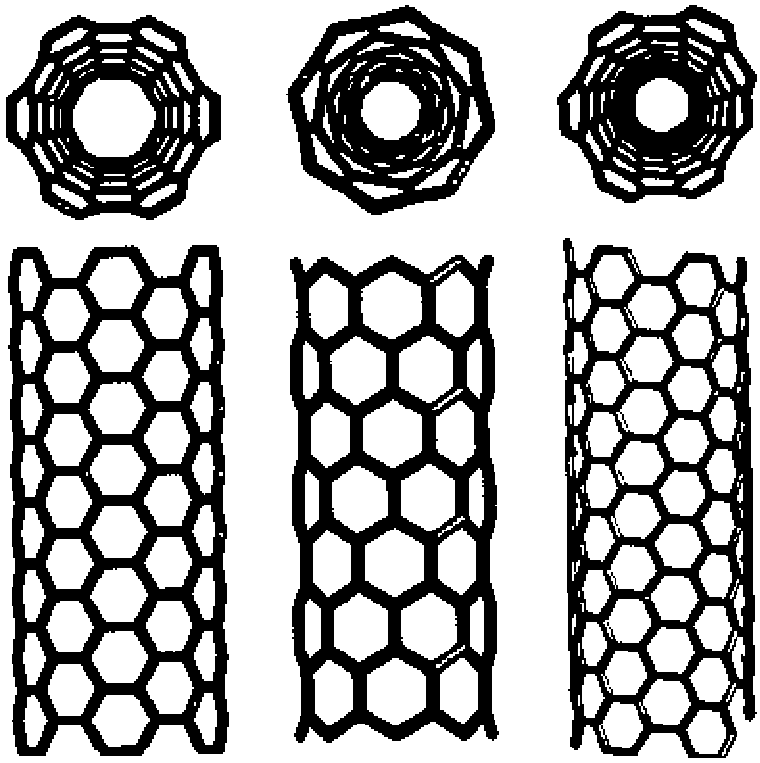

(a) (b) (c)

Figure 1.2: Different types of carbon nanotubes (a) Armchair (b) Zigzag and (c) Chiral

MWNTs are composed of a number of concentric SWNTs held together with relatively weak van der Waals forces. For MWNTs, the strength is limited by the ease with which individual graphene cylinders slide with respect to each other. Besides, the SWNTs are often in bundles of tens to hundreds of SWNT. Typically, the nanotubes are found to have self-organized into crystalline bundles, consisting of several to hundreds of SWNTs or MWNTs arranged in a closest-packed two-dimensional lattice. Within these bundles the nanotubes normally display a monodisperse range of diameters, with adjacent tubes weakly coupled via van der Waal interactions. However, the diameter of the CNTs is in the range of 0.4 nm to several hundred nm and the length ranges from several μm to several mm or even cm [4].

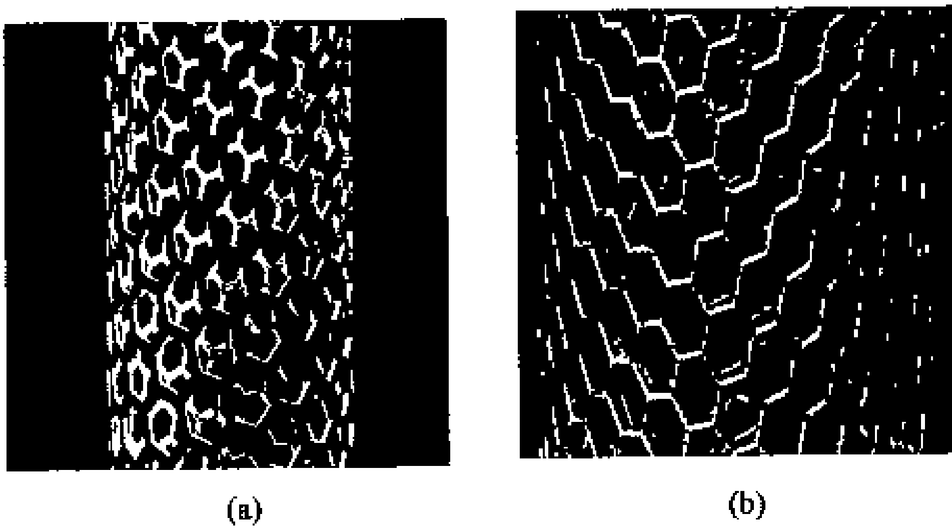

Figure 1.3: Carbon nanotubes (a) Single-walled nanotube (SWNT) (b) Multi-walled nanotube (MWNT)

1.2 PROPERTIES OF CARBON NANOTUBES

CNTs have remarkable mechanical, thermal and electrical properties. The properties of CNTs depend on atomic arrangement (how the sheets of graphite are 'rolled'), the diameter and length of the tubes, and the morphology of nanostructure. Mechanically, they are the stiffest known materials along with a predicted strength of about 100 times that of steel at only one-sixth of the weight. Recent theoretical calculations and direct experimental measurements showed that the elastic modulus of a SWNT is in the range of 1-5 TPa [5-7], which is significantly higher than that of a carbon fiber, from 0.1 to 0.8 TPa [8]. It has a breaking strength of about 37 GPa [9]. The MWNTs are reported to have lower mechanical performance than the SWNTs [4].

With regard to their thermal properties, CNTs are thermally stable up to 2800°C (in vacuum), exhibit a thermal conductivity about twice as high as diamond [10], and may exhibit a capacity to carry electric current a thousand times better than copper wires [11]. Furthermore, the chirality of the carbon nanotube has significant implications on the material properties. In particular, tube chirality is known to have a strong impact on the electronic properties of carbon nanotubes. CNTs can behave either as metals or semi-conductors depending on the arrangement of the carbon atoms [12-14]. In addition to their elastic and thermal properties, the bending of some CNTs has been found to be fully reversible up to a critical angle of 110° [15].

1.3 MOTIVATION OF THE PRESENT WORK

In view of their superior properties, CNTs show substantial promise for use as nanofibers to reinforce advanced composites. The large surface area of CNTs is also advantageous for mechanical bonding with the matrix in a composite. This, coupled with recent advances in nanotechnology and nanofabrication techniques, has triggered extensive research worldwide in the development and characterization of CNT-based multi-functional composites Many researchers have demonstrated that substantial improvements in the mechanical behaviors of polymers have been attained through the addition of small amounts of CNTs as a reinforcing phase. It is observed that when CNTs of about 1% weight are dispersed homogenously into polystyrene matrices the elastic modulus increases by 36-42% and the tensile strength improves by about 25% [16] It is also observed that the yield strength of multi-walled CNT/epoxy resin composites with a ductile matrix doubled with 1% weight of CNTs and quadrupled as the weight increased to 4% [17]. The mechanical load carrying capacities of CNTs in polymer composites have also been demonstrated in some experimental work [18–20] and numerical simulations [21]. All these investigations show that the load-carrying capacities of CNTs in a polymer matrix are significant and the CNT-based composites have the potential to provide extremely strong and ultra-light new materials.

However, much work still need to be done before the potentials of the CNT-based polymer composites can be fully realized in real engineering applications. Evaluating the effective material properties of such nanoscale materials is one of the challenging tasks for the development of nanocomposites. The degree of reinforcement observed in different experiments [16, 18-20] differs significantly.

Therefore, it is necessary to investigate which factors influence the reinforcement of the CNT-based polymer composites. Again, an interphase is unavoidable in the production of polymer matrix composites [22]. At the nanoscale, analytical models are difficult to establish or too complicated to solve, and tests are extremely difficult and expensive to conduct. Computational approach can play a significant role in the development of the CNT-based composites by providing simulation results to help on the understanding, analysis and design of such nanocomposites. Modeling and simulations of nanocomposites, on the other hand, can be achieved readily and cost effectively on even a desktop computer. Characterizing the mechanical properties of CNT-based polymer composites is just one of the many important and urgent tasks that simulations can accomplish Therefore the aim of the present work is to investigate the effective tensile elastic modulus (TEM) of CNT-based polymer composites for various physical conditions of CNTs and interphases developed during their fabrication with the help of simulation method.

1.4 OBJECTIVES

The specific objectives of the present research work are as follows:

(i) To study the effect of CNT diameter in case of perfect bonding between CNT and matrix on the effective tensile elastic modulus (TEM) of nanocomposite for both long and short fiber.

(ii) To examine the effect of CNT diameter in case of imperfect bonding between CNT and matrix on the effective TEM of nanocomposite for both Long and short fiber.

(iii) To identify the effect of CNT wall thickness on the effective TEM of the nanocomposite containing both short and long CNT for perfect bonding.

(iv) To investigate the effect of interphase thickness between CNT and matrix on the effective TEM of nanocomposite for both long and short CNT.

(v) To study the effect of CNT waviness ratio on the effective TEM of nanocomposite for a particular wavelength ratio.

(vi) To investigate the effect of CNT wavelength ratio on the effective TEM of nanocomposite for different waviness ratio.

CHAPTER 2
LITERATURE REVIEW

Sinnott et al. [29], Buongiorno Nardelli et al. [30] and Kang et al. [31] have provided abundant simulation results for understanding the behaviors of individual and bundled CNTs based on molecular dynamics (MD). Griebel and Hamackers [32] have also used MD to evaluate the elastic properties of single-walled CNT-based nanocomposites. However, MD simulations of CNTs are currently limited to very small length and time scales and cannot deal with the larger length scales in studying nanocomposites, due to the limitations of current computing power (for example, a $1\times1\times1$ μm^3 cube could contain up to 10^{12} atoms). Nanocomposites for engineering applications must expand from nano to micro, and eventually to macrolength scales. Therefore, continuum mechanics models can be applied for simulating the mechanical responses of the CNTs in a matrix, for studying the overall responses of CNT-based composites, before efficient large multiscale models are established.

The continuum mechanics approach has been employed for quite some time in the study of individual CNTs or CNT bundles to investigate their mechanical properties. The validity of the continuum approach to modeling of CNTs is still not fully established and the practice will continue to be questioned for some time to come. However, it seems to be the only feasible approach at present to obtain preliminary results for characterizing CNT-based composites using modeling and simulations. The best argument for using this continuum approach for now is simply the fact that it has been applied successfully for studying single or bundled CNTs, as given in Refs. [6, 33–37]. In these studies, the CNTs are considered as homogeneous and isotropic materials using continuum beam, shell, as well as 3-D solid models in the analyses of the deformation, buckling and dynamics responses of CNTs. Material properties such as equivalent Young's modulus and Poisson's ratios, and buckling modes of CNTs have been successfully predicted by using these continuum approaches. Qian et al. [38–40] have applied continuum mechanics for simulating the mechanical responses of individual or isolated CNTs which are treated as beams, thin shells or solids in cylindrical shapes. These studies suggest that the continuum mechanics approach can be applied safely to investigate the mechanical behaviors of the CNTs when the lengths of the CNTs are about 100 nm and above. Although successful to some extent and efficient in computation for models at larger length scales, continuum mechanics at this threshold faces the risk of breakdowns more than ever before, compared with the micromechanics simulations. The preferred approach for simulations of CNT-based composites should be a multiscale one where the MD and continuum mechanics are integrated in a computing environment that is detailed enough to account for the physics at nanoscales while efficient enough to handle nanocomposites at larger length scales. Before a multiscale approach for simulations of nanocomposites is successfully developed, the continuum mechanics approach seems to be the only feasible approach now for conducting some preliminary studies of such materials. However, cautions should be excised in applying the continuum approach, as discussed in Ref. [41]. Emphasis should be placed on the overall responses of CNTs or CNT-based composites, rather than on the local detailed phenomena, such as interfacial stresses or debonding, where the nanoscale MD approach should be employed.

Liu and Chen [42] investigated the interactions of the CNT with the matrix; interfacial stresses and load-carrying capabilities of the CNTs based on 3-D elasticity models. It is proposed that the 3-D elasticity models, instead of beam or shell models, should be used for the CNTs as well as the matrix, in order to ensure the accuracy and compatibility of the models for the CNTs and the matrix. One way to develop manageable 3-D continuum models for the study of CNT-based composites is to extend the concept of representative volume elements (RVEs) used for conventional fiber-reinforced composites at the microscale [43,44]. In this RVE approach, a single (or multiple) nanotube(s) with surrounding matrix material can be modeled, with properly applied boundary and interface conditions to account for the effects of the surrounding materials.

Liu and Chen [42] proposed three nanoscale RVEs (Fig. 2.1) based on 3-D elasticity theory for the study of CNT-based composites. They are the cylindrical RVE (Fig. 2.1(a)), square RVE (Fig. 2.1(b)) and hexagonal RVE (Fig. 2.1(c)). Under axisymmetric as well as antisymmetric loading, a 2-D axisymmetric model can be applied for the cylindrical RVE, which can significantly reduce the computational work [42]. Similar to the study of conventional fiber-reinforced composites [43], the square RVE models can be applied when the CNTs are arranged evenly in a square array, while the hexagonal RVE models can be applied when CNTs are in a hexagonal array, in the transverse direction. These RVEs can be used to study the interactions of a CNT with the matrix, such as the load transfer mechanism and stress distributions along the interfaces [42] or to evaluate the effective material properties of the CNT-based composites.

Liu and Chen [21] and Chen and Liu [45] used the concept of both cylindrical and square representative volume elements (RVEs) and used finite element and boundary element approaches to extract the required mathematical results. In their method, the CNT is modeled as a thin elastic layer in the form of either a capsule or open cylinder. Their study investigated the effective material properties (tensile moduli and Poisson's ratios) for various Young's moduli of matrices at particular volume fractions.

As mentioned earlier (Section 1.3), much work still need to be done before the potentials of the CNT-based polymer composites can be fully realized in real engineering applications. So, evaluation of the effective material properties of such nanoscale materials should be examined from different perspectives.

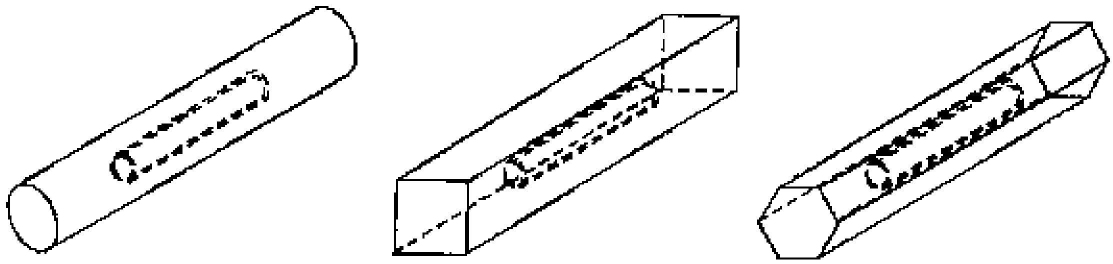

Figure 2.1: Three nanoscale RVEs for the analysis of CNT-based composites, (a) Cylindrical (b) Square and (c) Hexagonal

2.1 SUMMARY

From the above mentioned literature, it is found that the degree of nanotube reinforcement in polymer-based nanocomposites observed in different experiments [16, 18-20] differs significantly. Therefore, there is a need to investigate which factors influence the reinforcement of the polymer-based nanocomposites. However, diameter of CNTs may vary from one composite to another and interphase between the CNT and matrix (*i.e.* imperfect bonding) may develop during the fabrication of CNT-based composite. Also, the waviness and wavelength ratios of CNTs may differ from one composite to other. So the present work will study above effects on the effective TEM of polymer-based nanocomposites using the cylindrical RVEs and simulating through finite element method.

CHAPTER 3
THEORETICAL BACKGROUND

In this chapter, the governing equations for the applied mechanics with appropriate boundary conditions and also the solution procedure applicable for the present problem will be discussed. The generalized governing equations are based on constitutive relation of stress-strain and the equilibrium equations. Also, the finite element formulation of the axi-symmetric problem is presented in detail in this chapter. Again, the finite element software ANSYS 10.0 used to simulate the investigations is introduced later in this chapter.

3.1 FUNDAMENTAL EQUATIONS

The problem that dealt in this present study is axi-symmetric in nature. This problem is governed by the constitutive relation of stress-strain and the equilibrium equations. These constitutive relations and equilibrium equations are presented in detail in the following sections.

3.1.1 Stress-Strain Relations

For linear elastic materials, the stress-strain relations come from the generalized Hooke's law. For axi-symmetric model, the constitutive relation of stress, σ and strain, ε in the form of linear elasticity can be expressed as [46],

$$\sigma = \begin{Bmatrix} \sigma_r \\ \sigma_\theta \\ \sigma_z \\ \tau_{rz} \end{Bmatrix} = D\varepsilon \tag{3.1}$$

Where, D is the elasticity matrix; σ_r, σ_θ and σ_z are normal stress components at radial, circumferential and axial directions and τ_{rz} is the shear stress.

For isotropic materials, the two material properties are Young's modulus (or modulus of elasticity), E and Poisson's ratio, ν. If r and z denote respectively the radial and axial co-ordinates of a point, the generalized Hooke's law gives [46],

$$\begin{aligned} \varepsilon_r &= \frac{\sigma_r}{E} - \nu\frac{\sigma_\theta}{E} - \nu\frac{\sigma_z}{E} \\ \varepsilon_\theta &= -\nu\frac{\sigma_r}{E} + \frac{\sigma_\theta}{E} - \nu\frac{\sigma_z}{E} \\ \varepsilon_z &= -\nu\frac{\sigma_r}{E} - \nu\frac{\sigma_\theta}{E} + \frac{\sigma_z}{E} \\ \gamma_{rz} &= \frac{\tau_{rz}}{G} \end{aligned} \tag{3.2}$$

Where, $\varepsilon_z, \varepsilon_r$ and ε_θ are normal strain components at axial, radial and circumferential directions and γ_{zr} is the shear strain.

The shear modulus (or, modulus of rigidity), G is given by,

$$G = \frac{E}{2(1+\nu)} \tag{3.3}$$

Now, on solving for the stresses, the elasticity matrix, D becomes a symmetric (4×4) material matrix, given by,

$$D=\frac{E}{(1+\nu)(1-2\nu)}\begin{bmatrix}1-\nu & \nu & \nu & 0\\ \nu & 1-\nu & \nu & 0\\ \nu & \nu & 1-\nu & 0\\ 0 & 0 & 0 & 0.5-\nu\end{bmatrix} \tag{3.4}$$

The above mentioned matrix is used to calculate the stresses from strains in each element in finite element method.

3.1.2 The Equilibrium Equations

The equilibrium equations for the axi-symmetric problems can be expressed as,

$$\begin{aligned}&\frac{\partial\sigma_r}{\partial r}+\frac{\partial\tau_{rz}}{\partial z}+\frac{\sigma_r-\sigma_\theta}{r}+F_r=0\\&\frac{\partial\tau_{rz}}{\partial r}+\frac{\partial\sigma_z}{\partial z}+\frac{\tau_{rz}}{r}+F_z=0\end{aligned} \tag{3.5}$$

Where, F_r and F_z are the distributed body forces per unit volume [46].

The differential equations of equilibrium can be written as,

$$\overline{\nabla^T}\sigma+b=0 \tag{3.6}$$

Where, b is the body force vector.

The equations given here have to be solved by given certain boundary conditions. There are two types of boundary conditions, *i.e.* (a) mechanical boundary conditions prescribing stresses or surface tractions and (2) geometrical boundary conditions prescribing displacements. If a portion of the surface of the elastic body where stresses are prescribed by S_σ and the remaining surface where displacements are prescribed by S_u, then the whole surface of the elastic body can be denoted by [47],

$$S=S_\sigma+S_u \tag{3.7}$$

The mechanical boundary conditions on S_σ may be expressed in terms of prescribed traction vector t and the geometrical boundary conditions on S_u may be expressed in terms of prescribed displacement u.

It is no surprise that exact solutions for governing differential equations describing the engineering problems are generally difficult to obtain. This inability to obtain an exact solution of the problem may be attributed to either the complex nature of governing differential equations or the difficulties that arise from dealing with the boundary and initial conditions. To deal with such problems, numerical methods are adopted to obtain approximate solutions. Numerical methods approximate exact solution only at discrete points, called nodes. The first step of any numerical procedure is discretization. This process divides the medium of interest into a number of small sub regions and nodes. There are two common classes of numerical methods,

1. Finite difference method, and
2. Finite element method

With finite difference method, the differential equation is written for each node and the derivatives are replaced by difference equations. This approach results in a set of simultaneous linear equations. Although finite difference method is easy to understand and employ in simple problems, it is difficult to apply to problems with complex geometries or complex boundary conditions. This situation is also true for problems with no isotropic properties.

The advantage of the finite element method (FEM) is that, in principal, any problem can be solved, irrespective of the geometry and even considering complex constitutive relations. The expense that has to be paid for this gain in generality is that the FEM provides an approximate solution, which, however, converges towards the exact solution for a decreasing element size.

In this present numerical computation of the problem finite element method is used.

3.2 FINITE ELEMENT METHOD

The finite element method has become a powerful tool for the numerical solution of a wide range of engineering problems. Applications range from deformation and stress analysis of automotives, aircrafts, building and bridge structures to field analysis of heat fluxes, slippages and other flow problems. With the advances in computer technology and CAD systems, complex problems can be modeled with relative ease. Several alternative configurations can be tested on a computer before the first prototype is built. All of this suggests that we need to keep pace with these developments by understanding the basic theory, modeling techniques and computational aspects of the finite element method.

All the physical phenomena encountered in engineering mechanics are modeled by differential equations and usually the problem addressed is too complicated to be solved by classical analytical methods. The finite element method is a numerical approach by which general differential equations can be solved in an approximate manner.

The differential equations which describe the physical problem considered are assumed to hold over a certain region. This region may be one, two or three dimensional. It is a characteristic feature of the finite element method that instead of seeking approximations that hold directly over the entire region, the region is divided into smaller parts, so called finite elements and the approximation is then carried out over each element. For instance, even though the variable varies in a highly nonlinear in manner over the entire region, it may be for approximation to assume that the variable varies in a linear manner over each element. The collection of all elements is called a finite element mesh. The material properties and the governing relationships are considered over these elements and expressed in terms of unknown values at element corners.

When the type of approximation which is to be applied over each element has been selected, the corresponding behavior of each element can then be determined. This can be performed because the approximation made over each element is fairly simple. Having determined the behavior of all elements, these elements are then patched together, using some specific rules, to form the entire region, which eventually enable us to obtain an approximate solution for the behavior of the entire body.

Finite element method can be applied to obtain approximate solutions for arbitrary differential equations. For some physical problems differential equations can be solved by finite element method for both boundary value problem and the initial value problem.

A system with finite number of unknowns is called a discrete system in contrast to the original continuous system with an infinite number of unknowns. The determination of the values of the variable at the nodal points follows from the solution of a certain system of equations. A system often involves thousands of equations, so such systems cannot be solved by hand therefore the FEM relies entirely on the availability of efficient computers.

The finite element method can be applied arbitrary differential equations and arbitrary geometries of bodies consisting arbitrary materials. It is therefore no surprise that the FEM today is the most powerful approach for solving differential equations that occur in engineering, physics and mathematics.

In the next section, the axi-symmetric modeling of finite element method will be discussed as for the analysis made in this research work. The formulation and equations used to analyze the axi-symmetric finite element problem is discussed below.

3.2.1 Finite Element Formulation

It is mentioned earlier, the problem dealt in this present research work is axi-symmetric in nature. So, this section deals with the formulation of finite element equations for axi-symmetric problems. Due to symmetry about the axis of revolution, such problems can be solved using two-dimensional elements and all boundary conditions are independent of the circumferential coordinate θ. So, the displacement field is independent of the circumferential or tangential coordinate θ. Hence, the stress analysis is mathematically two-dimensional, even though the physical problem is three-dimensional. We cannot ignore the tangential coordinate completely, however, since there is strain in the tangential direction. Note that, in the radial direction, the element undergoes displacement, which introduces increase in circumference and associated circumferential strain.

If u, v and w are displacements in the radial, tangential (circumferential) and axial directions respectively, then the displacement vector can be expressed as,

$$u = \begin{Bmatrix} u \\ v \\ w \end{Bmatrix} \tag{3.8}$$

As the displacement field is independent of the circumferential or tangential coordinate θ for axi-symmetric problems, Eq. (3.8) can be expressed as [48],

$$u = \begin{Bmatrix} u \\ w \end{Bmatrix} \tag{3.9}$$

The stresses and strains are given by,

$$\begin{aligned} \sigma &= \begin{bmatrix} \sigma_r & \sigma_\theta & \sigma_z & \tau_{rz} \end{bmatrix}^T \\ \varepsilon &= \begin{bmatrix} \varepsilon_r & \varepsilon_\theta & \varepsilon_z & \gamma_{rz} \end{bmatrix}^T \end{aligned} \tag{3.10}$$

The stress-strain relations are given by, from Eq. (3.1), as,

$$\sigma = D\varepsilon \tag{3.11}$$

Where, D is a (4×4) symmetric matrix. For isotropic materials, D is given by Eq. (3.4).

The strain-displacement relations are given by [46],

$$\varepsilon = \begin{Bmatrix} \varepsilon_r \\ \varepsilon_\theta \\ \varepsilon_z \\ \gamma_{rz} \end{Bmatrix} = \begin{Bmatrix} \dfrac{\partial u}{\partial r} \\ \dfrac{u}{r} \\ \dfrac{\partial w}{\partial z} \\ \dfrac{\partial u}{\partial z} + \dfrac{\partial w}{\partial r} \end{Bmatrix} \tag{3.12}$$

Now, for the formulation of finite element method, the symmetric area is divided into eight-node quadrilateral elements, with four corner nodes and four mid-side nodes. Let, the four corner nodes are denoted as 1, 2, 3 & 4 and the other four mid-side nodes are denoted as 5, 6, 7 & 8. Each node has two degrees of freedom of translation along radial and axial axis.

Now, using the eight-node quadrilateral element with nodes numbered in the anti-clockwise sense, from the isoparametric formulation, the geometric expressions become [48],

$$\begin{aligned} r &= \sum_{i=1}^{8} N_i(r,z) r_i \\ z &= \sum_{i=1}^{8} N_i(r,z) z_i \end{aligned} \tag{3.13}$$

With the coordinates of node i is (r_i, z_i) and refer to the global coordinate system.

And the displacement field can be expressed as,

$$u(r,z)=\sum_{i=1}^{8}N_i(r,z)u_i$$
$$w(r,z)=\sum_{i=1}^{8}N_i(r,z)w_i \tag{3.14}$$

With, u_i and w_i representing the nodal radial and axial displacements, respectively and N_i representing the shape function or interpolation function.

The expression of the interpolation function, N_i (r, z) in terms of the nodal coordinates is algebraically complex. Fortunately, the complexity can be reduced by a more judicious choice of coordinates, which is known as natural coordinates or serendipity coordinates s and t. Here, s and t can be expressed as [48],

$$s=\frac{r-\bar{r}}{a}$$
$$t=\frac{z-\bar{z}}{b} \tag{3.15}$$

Where, $2a$ and $2b$ are the width and height of the rectangle, respectively and the coordinates of the centroid are,

$$\bar{r}=\frac{r_1+r_2}{2}$$
$$\bar{z}=\frac{z_1+z_2}{2} \tag{3.16}$$

Therefore, s and t are such that the values range from -1 to +1.

So, the geometric expression of Eq. (3.13) can be written as,

$$r=\sum_{i=1}^{8}N_i(s,t)r_i$$
$$z=\sum_{i=1}^{8}N_i(s,t)z_i \tag{3.17}$$

And the displacement field of Eq. (3.14) can be written as,

$$u(r,z)=\sum_{i=1}^{8}N_i(s,t)u_i$$
$$w(r,z)=\sum_{i=1}^{8}N_i(s,t)w_i \tag{3.18}$$

Applying the conditions that must be satisfied by each interpolation function at each node, it can be expressed for the four corner nodes of the eight-node quadrilateral element as [48],

$$\begin{aligned}
N_1(s,t)&=\frac{1}{4}(1-s)(1-t)(-s-t-1)\\
N_2(s,t)&=\frac{1}{4}(1+s)(1-t)(s-t-1)\\
N_3(s,t)&=\frac{1}{4}(1+s)(1+t)(s+t-1)\\
N_4(s,t)&=\frac{1}{4}(1-s)(1+t)(-s+t-1)
\end{aligned} \tag{3.19}$$

The form of the interpolation functions associated with the mid-side nodes can be expressed as,

$$\begin{aligned}
N_5(s,t)&=\frac{1}{2}(1-s^2)(1-t)\\
N_6(s,t)&=\frac{1}{2}(1+s)(1-t^2)\\
N_7(s,t)&=\frac{1}{2}(1-s^2)(1+t)\\
N_8(s,t)&=\frac{1}{2}(1-s)(1-t^2)
\end{aligned} \tag{3.20}$$

So, the components of the displacement vector, i.e. Eq. (3.9), can be expressed as,

$$u=\begin{Bmatrix} u \\ w \end{Bmatrix}=[N]\{\delta\} \tag{3.21}$$

Where, N is a (2×16) matrix, given by,

$$N = \begin{bmatrix} N_1 & 0 & N_2 & 0 & N_3 & 0 & N_4 & 0 & N_5 & 0 & N_6 & 0 & N_7 & 0 & N_8 & 0 \\ 0 & N_1 & 0 & N_2 & 0 & N_3 & 0 & N_4 & 0 & N_5 & 0 & N_6 & 0 & N_7 & 0 & N_8 \end{bmatrix}$$

And δ is a (16×1) matrix, which is determined by the two displacement vectors at the eight nodal points of the quadrilateral element, given by,

$$\delta = \begin{bmatrix} u_1 & w_1 & u_2 & w_2 & u_3 & w_3 & u_4 & w_4 & u_5 & w_5 & u_6 & w_6 & u_7 & w_7 & u_8 & w_8 \end{bmatrix}^T \quad (3.22)$$

Now, the strain components can be expressed as [48],

$$\begin{aligned} \varepsilon_r &= \frac{\partial u}{\partial r} = \sum_{i=1}^{8} \frac{\partial N_i}{\partial r} u_i \\ \varepsilon_\theta &= \frac{u}{r} = \sum_{i=1}^{8} \frac{N_i}{r} u_i \\ \varepsilon_z &= \frac{\partial w}{\partial z} = \sum_{i=1}^{8} \frac{\partial N_i}{\partial z} w_i \\ \gamma_{rz} &= \frac{\partial u}{\partial z} + \frac{\partial w}{\partial r} = \sum_{i=1}^{8} \frac{\partial N_i}{\partial z} u_i + \sum_{i=1}^{8} \frac{\partial N_i}{\partial r} w_i \end{aligned} \quad (3.23)$$

So, the strain-displacement relations of Eq. (3.12) can be written as,

$$\varepsilon = \begin{Bmatrix} \varepsilon_r \\ \varepsilon_\theta \\ \varepsilon_z \\ \gamma_{rz} \end{Bmatrix} = [B]\{\delta\} \quad (3.24)$$

Where, B is a (4×16) matrix, given by,

$$B=\begin{bmatrix} \frac{\partial N_1}{\partial r} & 0 & \frac{\partial N_2}{\partial r} & 0 & \frac{\partial N_3}{\partial r} & 0 & \frac{\partial N_4}{\partial r} & 0 & \frac{\partial N_5}{\partial r} & 0 & \frac{\partial N_6}{\partial r} & 0 & \frac{\partial N_7}{\partial r} & 0 & \frac{\partial N_8}{\partial r} & 0 \\ \frac{N_1}{r} & 0 & \frac{N_2}{r} & 0 & \frac{N_3}{r} & 0 & \frac{N_4}{r} & 0 & \frac{N_5}{r} & 0 & \frac{N_6}{r} & 0 & \frac{N_7}{r} & 0 & \frac{N_8}{r} & 0 \\ 0 & \frac{\partial N_1}{\partial z} & 0 & \frac{\partial N_2}{\partial z} & 0 & \frac{\partial N_3}{\partial z} & 0 & \frac{\partial N_4}{\partial z} & 0 & \frac{\partial N_5}{\partial z} & 0 & \frac{\partial N_6}{\partial z} & 0 & \frac{\partial N_7}{\partial z} & 0 & \frac{\partial N_8}{\partial z} \\ \frac{\partial N_1}{\partial z} & \frac{\partial N_1}{\partial r} & \frac{\partial N_2}{\partial z} & \frac{\partial N_2}{\partial r} & \frac{\partial N_3}{\partial z} & \frac{\partial N_3}{\partial r} & \frac{\partial N_4}{\partial z} & \frac{\partial N_4}{\partial r} & \frac{\partial N_5}{\partial z} & \frac{\partial N_5}{\partial r} & \frac{\partial N_6}{\partial z} & \frac{\partial N_6}{\partial r} & \frac{\partial N_7}{\partial z} & \frac{\partial N_7}{\partial r} & \frac{\partial N_8}{\partial z} & \frac{\partial N_8}{\partial r} \end{bmatrix}$$

And, δ is a (16×1) matrix, as given in Eq. (3.22).

Now, the components $\partial N_i/\partial r$ and $\partial N_i/\partial z$ to be computed. Since the interpolation functions are expressed in (s, t) coordinates, these derivatives can be written as [48],

$$\begin{aligned} \frac{\partial N_i}{\partial r} &= \frac{\partial N_i}{\partial s}\frac{\partial s}{\partial r}+\frac{\partial N_i}{\partial t}\frac{\partial t}{\partial r} \\ \frac{\partial N_i}{\partial z} &= \frac{\partial N_i}{\partial s}\frac{\partial s}{\partial z}+\frac{\partial N_i}{\partial t}\frac{\partial t}{\partial z} \end{aligned} \tag{3.25}$$

However, unless the relations in Eq. (3.17) are inverted, the partial derivatives of the natural coordinates with respect to the global coordinates are not known. As it is virtually impossible to invert Eq. (3.17) to explicit algebraic expressions, a different approach must be taken.

However, the partial derivatives of each interpolation function can be expressed as [48],

$$\begin{aligned} \frac{\partial N_i}{\partial s} &= \frac{\partial N_i}{\partial r}\frac{\partial r}{\partial s}+\frac{\partial N_i}{\partial z}\frac{\partial z}{\partial s} \\ \frac{\partial N_i}{\partial t} &= \frac{\partial N_i}{\partial r}\frac{\partial r}{\partial t}+\frac{\partial N_i}{\partial z}\frac{\partial z}{\partial t} \end{aligned} \tag{3.26}$$

Where, the value of i ranges from 1 to 8.

Writing Eq. (3.26) in matrix form,

$$\begin{Bmatrix} \dfrac{\partial N_i}{\partial s} \\ \dfrac{\partial N_i}{\partial t} \end{Bmatrix} = \begin{bmatrix} \dfrac{\partial r}{\partial s} & \dfrac{\partial z}{\partial s} \\ \dfrac{\partial r}{\partial t} & \dfrac{\partial z}{\partial t} \end{bmatrix} \begin{Bmatrix} \dfrac{\partial N_i}{\partial r} \\ \dfrac{\partial N_i}{\partial z} \end{Bmatrix} \tag{3.27}$$

Where, the value of i ranges from 1 to 8.

It is observed that the (2×1) vector on the left-hand side is known, since the interpolation functions are expressed explicitly in the natural coordinates. Similarly, the terms in the (2×2) coefficient matrix on the right-hand side are known via Eq. (3.17). The latter, known as the *Jacobian* matrix, denoted [J], is given by [48],

$$[J] = \begin{bmatrix} \dfrac{\partial r}{\partial s} & \dfrac{\partial z}{\partial s} \\ \dfrac{\partial r}{\partial t} & \dfrac{\partial z}{\partial t} \end{bmatrix} = \begin{bmatrix} \sum_{i=1}^{8} \dfrac{\partial N_i}{\partial s} r_i & \sum_{i=1}^{8} \dfrac{\partial N_i}{\partial s} z_i \\ \sum_{i=1}^{8} \dfrac{\partial N_i}{\partial t} r_i & \sum_{i=1}^{8} \dfrac{\partial N_i}{\partial t} z_i \end{bmatrix} \tag{3.28}$$

If the inverse of the *Jacobian* matrix can be determined, Eq. (3.27) can be solved for the partial derivatives of the interpolation functions with respect to the global coordinates to obtain [48],

$$\begin{Bmatrix} \dfrac{\partial N_i}{\partial r} \\ \dfrac{\partial N_i}{\partial z} \end{Bmatrix} = [J]^{-1} \begin{Bmatrix} \dfrac{\partial N_i}{\partial s} \\ \dfrac{\partial N_i}{\partial t} \end{Bmatrix} = \begin{bmatrix} I_{11} & I_{12} \\ I_{21} & I_{22} \end{bmatrix} \begin{Bmatrix} \dfrac{\partial N_i}{\partial s} \\ \dfrac{\partial N_i}{\partial t} \end{Bmatrix} \tag{3.29}$$

Where, the value of i ranges from 1 to 8 and the terms of the inverse of the *Jacobian* matrix denoted I_{ij} for convenience.

The elemental area $dA = drdz$ can be transformed in the natural coordinate system, given by [48],

$$dA = drdz = \det\left[J\right] dsdt = \left|J\right| dsdt \tag{3.30}$$

Now, the element stiffness matrix will be calculated. Element stiffness matrix is important to obtain the value of displacement in each element of FE method.

The total strain energy of the element is given by [47],

$$\begin{aligned} U_e &= \frac{1}{2} \iiint_{V_e} \{\varepsilon\}^T [D]\{\varepsilon\} dV_e = \frac{1}{2} \iiint_{V_e} \{\delta\}^T [B]^T [D][B]\{\delta\} dV_e \\ &= \frac{1}{2}\{\delta\}^T \iiint_{V_e} [B]^T [D][B] dV_e \{\delta\} = \frac{1}{2}\{\delta\}^T [k]\{\delta\} \end{aligned} \tag{3.31}$$

Where, V_e is the total volume of the element and $[k]$ is the element stiffness matrix defined by [47],

$$[k] = \iiint_{V_e} [B]^T [D][B] dV_e = \iiint [B]^T [D][B] r dr d\theta dz \tag{3.32}$$

For axial symmetry, the integrand is independent of the circumferential coordinate θ, so the integration indicated in Eq. (3.32) becomes,

$$[k] = 2\pi \iint_{A_e} [B]^T [D][B] r dr dz \tag{3.33}$$

Using Eq. (3.30), the stiffness matrix, $[k]$ in Eq. (3.33) can be written in terms of natural coordinates as,

$$[k] = 2\pi \int_{-1}^{1}\int_{-1}^{1} [B]^T [D][B] |J| \left(as + \bar{r}\right) dsdt \tag{3.34}$$

Where, a is half of the width of the element and $\bar{r}$ is r-coordinate of the element midpoint. This element stiffness matrix is required to obtain the displacements in each node of an element.

Now, the force terms will be calculated. Axi-symmetric problems often involve surface forces in the form of internal pressure and body forces arising from rotation of the body and gravity. In each case, the external influences are reduced to nodal forces using the work equivalence concept.

Let, the eight-node quadrilateral axi-symmetric element is subjected to pressures P_r and P_z in the radial and axial directions. The equivalent nodal forces can be expressed as [48],

$$f^p = 2\pi \int_S [N]^T \begin{Bmatrix} p_r \\ p_z \end{Bmatrix} r dS \tag{3.35}$$

Where, dS is the differential length of the element edge in question and located at a radial distance r from the axis of symmetry. The area on which pressure components act is $2\pi r dS$. Here, the force vector in Eq. (3.35) is given by,

$$f^p = \begin{bmatrix} f_{1x}^p & f_{1y}^p & f_{2x}^p & f_{2y}^p & f_{3x}^p & f_{3y}^p & f_{4x}^p & f_{4y}^p & f_{5x}^p & f_{5y}^p & f_{6x}^p & f_{6y}^p & f_{7x}^p & f_{7y}^p & f_{8x}^p & f_{8y}^p \end{bmatrix}^T \tag{3.36}$$

And the interpolation function can be expressed as in Eq. (3.37),

Now, body forces acting on the eight-node axi-symmetric element will be calculated. Let the body forces (force per unit mass) R_B and Z_B act in the radial and axial directions, respectively.

$$[N]^T = \begin{bmatrix} N_1 & 0 \\ 0 & N_1 \\ N_2 & 0 \\ 0 & N_2 \\ N_3 & 0 \\ 0 & N_3 \\ N_4 & 0 \\ 0 & N_4 \\ N_5 & 0 \\ 0 & N_5 \\ N_6 & 0 \\ 0 & N_6 \\ N_7 & 0 \\ 0 & N_7 \\ N_8 & 0 \\ 0 & N_8 \end{bmatrix} \tag{0.37}$$

Then the equivalent nodal forces can be expressed as [48],

$$f^B = 2\pi\rho \iint_A [N]^T \begin{Bmatrix} R_B \\ R_B \end{Bmatrix} r\,dr\,dz \tag{0.38}$$

Where, the body force vector is similar to Eq. (3.36) and the interpolation function is given by Eq. (3.37).

Now, total potential energy of an element can be expressed as [47],

$$\Pi = U_e - W = \frac{1}{2}\{\delta\}^T [k]\{\delta\} - \{\delta\}^T \{f\} \tag{0.39}$$

The element nodal force vector is defined in the column matrix,

$$f = \begin{bmatrix} f_{1r} & f_{1z} & f_{2r} & f_{2z} & f_{3r} & f_{3z} & f_{4r} & f_{4z} & f_{5r} & f_{5z} & f_{6r} & f_{6z} & f_{7r} & f_{7z} & f_{8r} & f_{8z} \end{bmatrix}^T \tag{3.40}$$

The force vector in Eq. (3.40) may include the directly applied external forces at nodes, the work-equivalent nodal forces corresponding to body forces and forces arising from applied pressure on element faces.

Now, the total potential energy for an element must be minimum and for this minimum potential energy,

$$\frac{\partial \Pi}{\partial \delta_i} = 0 \tag{3.41}$$

Where, the values of i ranges from 1 to 8.

If the indicated mathematical operations of Eq. (3.41) are carried out on Eq. (3.39), the result is the matrix relation, given by,

$$[k]\{\delta\} = \{f\} \tag{3.42}$$

Once the element characteristics, namely, the element matrices and element vectors, are found in a common global coordinate system, the next step is to construct the overall or system equations. The procedure for constructing the system equations from the element characteristics is the same regardless of the type of problem and the number and type of elements used.

Let, the assembled global equations are of the form,

$$[K]\{\Delta\} = \{F\} \tag{3.43}$$

Where, $[K]$ representing the assembled global stiffness matrix, $\{\Delta\}$ representing the global nodal displacement vector and $\{F\}$ representing the global nodal force vector. The nodal forces may include directly applied external forces at nodes, the work-equivalent nodal forces corresponding to body forces and forces arising from applied pressure on element faces.

The above equation gives a set of equations for each node of an element and for all the elements of a discretized body, which are obtained previously. Then all the equations are solved by applying appropriate boundary conditions to them and the values of displacements are obtained from the known stiffness matrix and force terms are obtained from boundary conditions.

This is the procedure of solving axi-symmetric models using finite element method. Now, solving of these equations requires computer as these large volumes of equations is not possible to solve by hand. So, in the next section, the computer program and software used for solving these problems are discussed.

3.3 FINITE ELEMENT SOFTWARE

Computer use is an essential part of the finite element analysis. Well-developed, well-maintained and well-supported computer programs are necessary in solving engineering problems and interpreting results. Many available commercial finite element packages fulfill these needs. It is also the trend in industry that the results are acceptable only when solved using certain standard computer program packages. The commercial packages provide user-friendly data-input platforms and elegant and easy to follow display formats. However, the packages do not provide an insight into the formulations and solution methods. Specially developed computer programs with available source codes enhance the learning process. In this research work, ANSYS 10.0 is used to model the problems which is a popular general-purpose finite element software.

3.3.1 General Description of the Software

ANSYS 10.0 is a comprehensive general-purpose finite element computer program that contains over 100,000 lines of code. ANSYS 10.0 is capable of performing static, dynamic, heat transfer, fluid flow and electromagnetism analyses. ANSYS 10.0 has been a leading FE analysis program for well over 20 years. Today, ANSYS 10.0 is used in many engineering fields, including aerospace, automotives, electronics and nuclear. In order to use ANSYS 10.0 or any other "canned" FE analysis computer program intelligently, it is imperative that one first fully understand the underlying basic concepts and limitations of the finite element methods. ANSYS 10.0 is a very powerful and impressive engineering tool that may be used to solve a variety of problems.

3.3.2 Basic Steps in the Finite Element Method

The basic steps involved in any finite element analysis consist of the following [47]:

Preprocessing Phase

1. Create and discretize the solution domain into finite elements; that is, subdivide the problem into nodes and elements.
2. Assume a shape function to represent the physical behavior of an element; that is, an approximate continuous function is assumed to represent the solution of an element.
3. Develop equations for an element.
4. Assemble the elements to present the entire problem. Contrast the global stiffness matrix.
5. Apply boundary conditions, initial conditions and loading.

Solution Phase

6. Solve a set of linear or nonlinear algebraic equations simultaneously to obtain nodal results. Such as displacement values at different nodes or temperature values at different nodes in a heat transfer problem.

Postprocessing Phase

7. Obtain other important information. At this point, you may be interested in values of principal stresses, heat fluxes, etc.

ANSYS 10.0 uses the same procedure to solve any problem.

3.3.3 Two Dimensional Axi-symmetric Elements Used in the Software

A number of two dimensional axi-symmetric elements are used in ANSYS 10.0; among them some are used for solving solid mechanics problems. Some of these structural elements are described below [47].

PLANE42 is used for 2-D modeling of solid structures. The element can be used either as a plane element (plane stress or plane strain) or as an axi-symmetric element. The element is defined by four nodes having two degrees of freedom at each node: translations in the nodal x and y directions. The element may be used to analyze plasticity, creep, swelling, stress stiffening, large deflection, and large strain. The geometry of PLANE42 element is shown in Fig. 3.1.

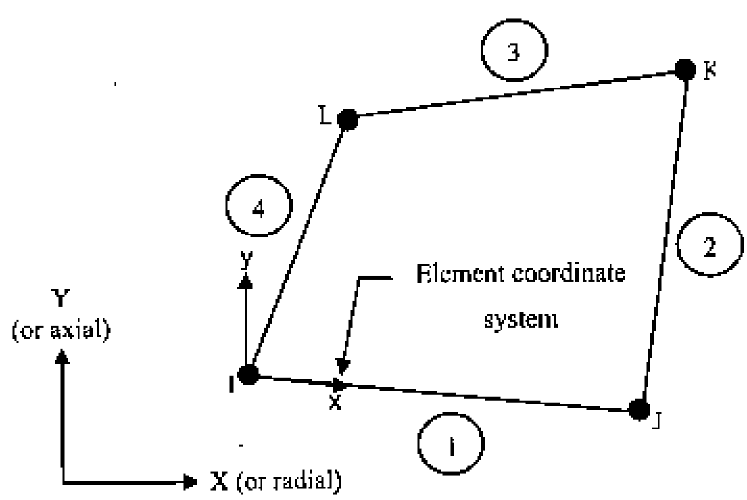

Figure 3.1: PLANE42 element used by ANSYS 10.0

PLANE82 is a higher order version of the 2-D, four-node element (PLANE42). It provides more accurate results for mixed (quadrilateral-triangular) automatic meshes and can tolerate irregular shapes without as much loss of accuracy. The 8-node elements have compatible displacement shapes and are well suited to model curved boundaries. The 8-node element is defined by eight nodes having two degrees of freedom at each node: translations in the nodal x and y directions. The element may be used as a plane element or as an axi-symmetric element. The element has plasticity, creep, swelling, stress stiffening, large deflection, and large strain capabilities. Fig. 3.2 shows the geometry of PLANE82 element.

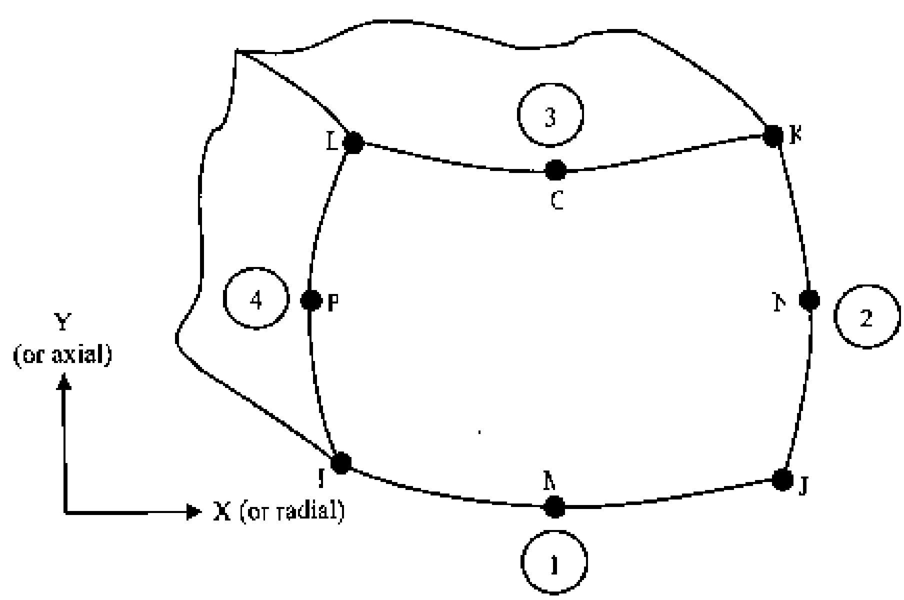

Figure 3.2: PLANE82 element nsed by ANSYS 10.0

PLANE83 is nsed for 2-D modeling of axi-symmetric structures with nonaxi-symmetric loading. Examples of such loading are bending, shear, or torsion. The element has three degrees of freedom per node: translations in the nodal x, y, and z directions. For unrotated nodal coordinates, these directions correspond to the radial, axial, and tangential directions, respectively. It provides accurate results for mixed (quadrilateral-triangular) automatic meshes and can tolerate irregular shapes without as much loss of accnracy. The element is also a generalization of the axi-symmetric version of PLANE82, the 2-D 8-node structural solid element, in that the loading need not be axi-symmetric. The geometry of PLANE83 element is shown in Fig. 3.3.

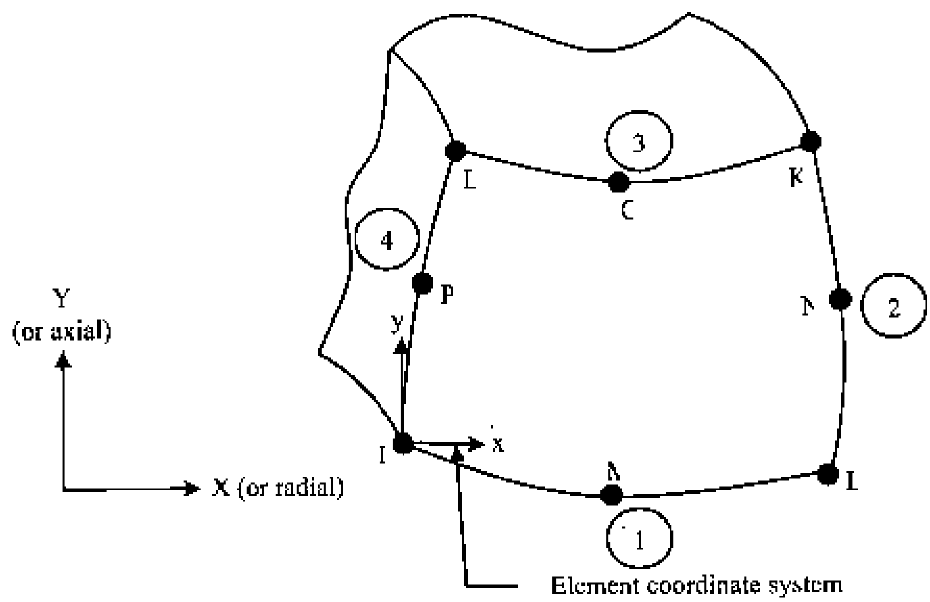

Figure 3.3: PLANE83 element used by ANSYS 10.0

PLANE182 is used for 2-D modeling of solid structures. The element can be used as either a plane element (plane stress, plane strain or generalized plane strain) or an axi-symmetric element. It is defined by four nodes having two degrees of freedom at each node: translations in the nodal x and y directions. The element has plasticity, hyperelasticity, stress stiffening, large deflection, and large strain capabilities. It also has mixed formulation capability for simulating deformations of nearly incompressible elastoplastic materials, and fully incompressible hyperelastic materials. Fig. 3.4 shows the geometry of PLANE182 element.

PLANE183 is a higher order 2-D, 8-node element. PLANE183 has quadratic displacement behavior and is well suited to modeling irregular meshes (such as those produced by various CAD/CAM systems).

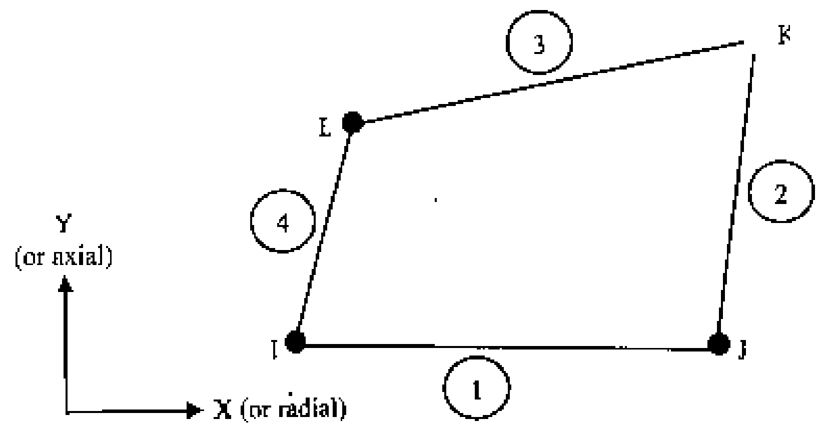

Figure 3.4: PLANE182 element used by ANSYS 10.0

This element is defined by 8 nodes having two degrees of freedom at each node: translations in the nodal x and y directions. The element may be used as a plane element (plane stress, plane strain and generalized plane strain) or as an axi-symmetric element. This element has plasticity, hyperelasticity, creep, stress stiffening, large deflection, and large strain capabilities. It also has mixed formulation capability for simulating deformations of nearly incompressible elastoplastic materials, and fully incompressible hyperelastic materials. Fig. 3.5 shows the geometry of PLANE183 element.

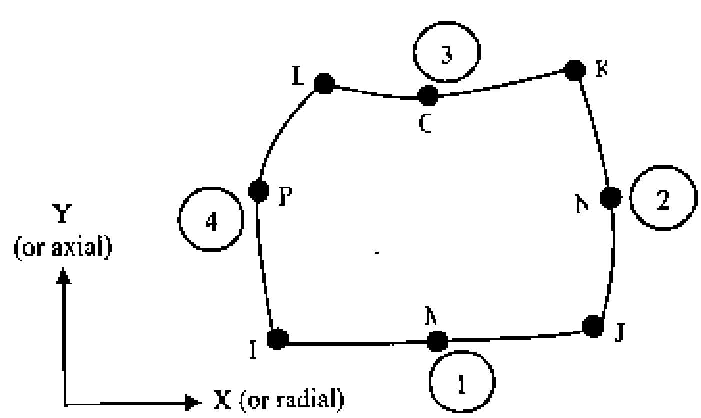

Figure 3.5: PLANE183 element used by ANSYS 10.0

In the present study PLANE82 is used to describe the two dimensional axi-symmetric models. This element is suitable for analyzing the models having axi-symmetric shape with axi-symmetric loading. In the next section, the methods ANSYS 10.0 uses to solve equations, described in section 3.2, are discussed.

3.3.4 The Frontal Solver

There are number of solver used by the software ANSYS 10.0 to solve the equations of a given problem such as, Frontal Solver (direct elimination solver), Sparse Direct Solver (direct elimination solver), Preconditioned Conjugate Gradient (PCG) Solver (iterative solver), Incomplete Cholesky Conjugate Gradient (ICCG) Solver (iterative solver) and Jacobi Conjugate Gradient (JCG) Solver (iterative solver) [47]. The frontal solver is the default, but one can select a different solver. In the present study the frontal solver method is used to get the solution.

The frontal solver does not assemble the complete global matrix. Instead, ANSYS 10.0 performs the assembly and solution steps simultaneously as the solver processes each element.

The method works as follows:

- After the individual element matrices are calculated, the solver reads in the degrees of freedom (DOF) for the first element. These are written on .EMAT file.
- The program eliminates any degrees of freedom that can be expressed in terms of the other DOF by writing an equation to the .TRI file. This process repeats for all elements until all degrees of freedom have been eliminated and a complete triangularized matrix is left on the .TRI file.
- The program then calculates the nodal DOF solution by back substitution, and uses the individual element matrices to calculate the element solution. Fig. 3.6 shows the main steps involved in a frontal solution and the files produced at each step [47].

These steps are shown in the following Fig. 3.6.

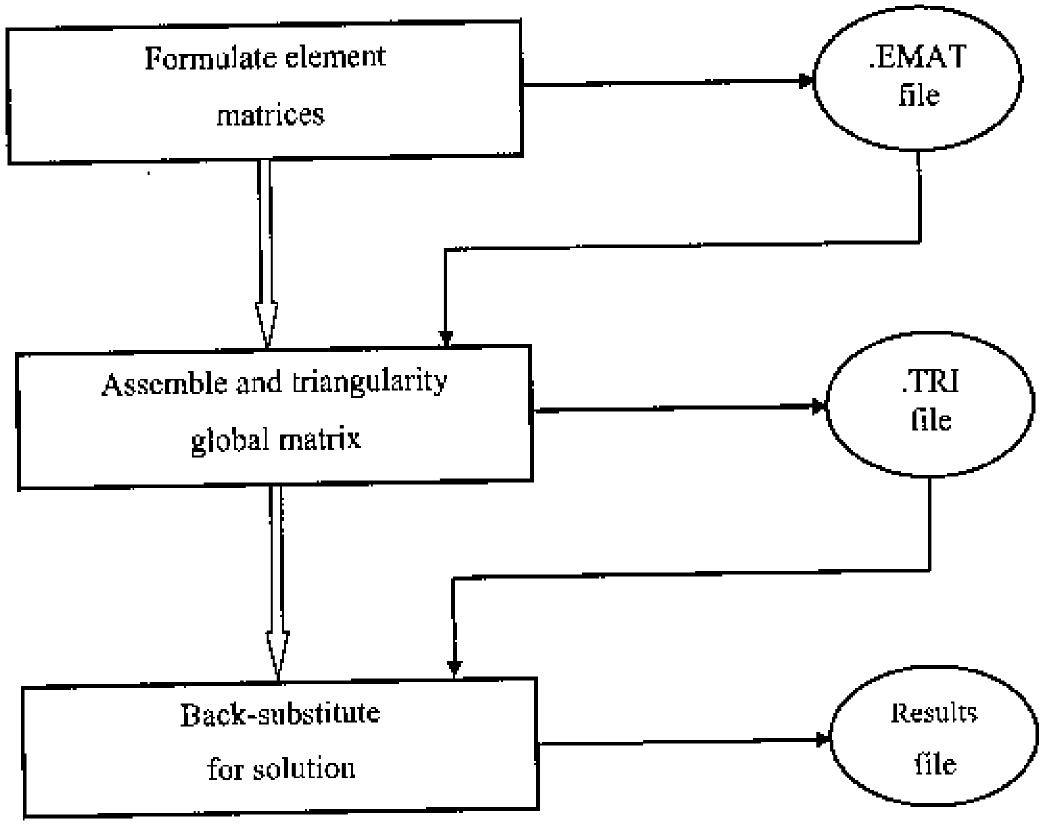

Figure 3.6: Typical steps and files in a frontal solution

CHAPTER 4
COMPUTATIONAL DETAILS

In this chapter, the cylindrical representative volume elements (RVEs), used to investigate the effective tensile elastic modulus (TEM) and the formulas used to process the output of finite element analysis using ANSYS 10.0 to evaluate the effective material constant is presented in details. Besides, the analytical solutions based on the strength of materials theory developed by [21] are presented for both long and short CNT based RVEs for comparison with the FEM results. Also, the modeling of the representative volume element in ANSYS 10.0 is presented sequentially.

4.1 RVEs FOR EVALUATION OF THE EFFECTIVE MATERIAL PROPERTY

CNTs are in different sizes and forms when they are dispersed in a matrix to make a nanocomposite. They can be single-walled or multi-walled with length of a few nanometers or a few micrometers, and can be straight, twisted and curled, or in the form of ropes [10]. Their distribution and orientation in the matrix can be uniform and unidirectional (which may be the ultimate goal) or random. All these factors make the simulations of CNT-based composites extremely difficult. As mentioned in chapter 2, the concept of unit cells or representative volume elements, which have been applied successfully in the studies of conventional fiber-reinforced composites at the microscale, can be extended to study the CNT-based composites at the nanoscale. In the present study, 3-D nanoscale cylindrical RVEs are employed to investigate the various effects on the tensile elastic modulus of nanocomposites. Various effects are studied on nanocomposites containing both short and long CNTs The 3-D nanoscale RVEs containing long and short CNTs are shown in Fig. 4.1 and 4.2 respectively. Figure 4.2 shows the one-half view of the model in which it is seen that short fiber has hemispherical end caps at both end. Figure 4.1 also shows that the models are axi-symmetric with respect to Z-axis.

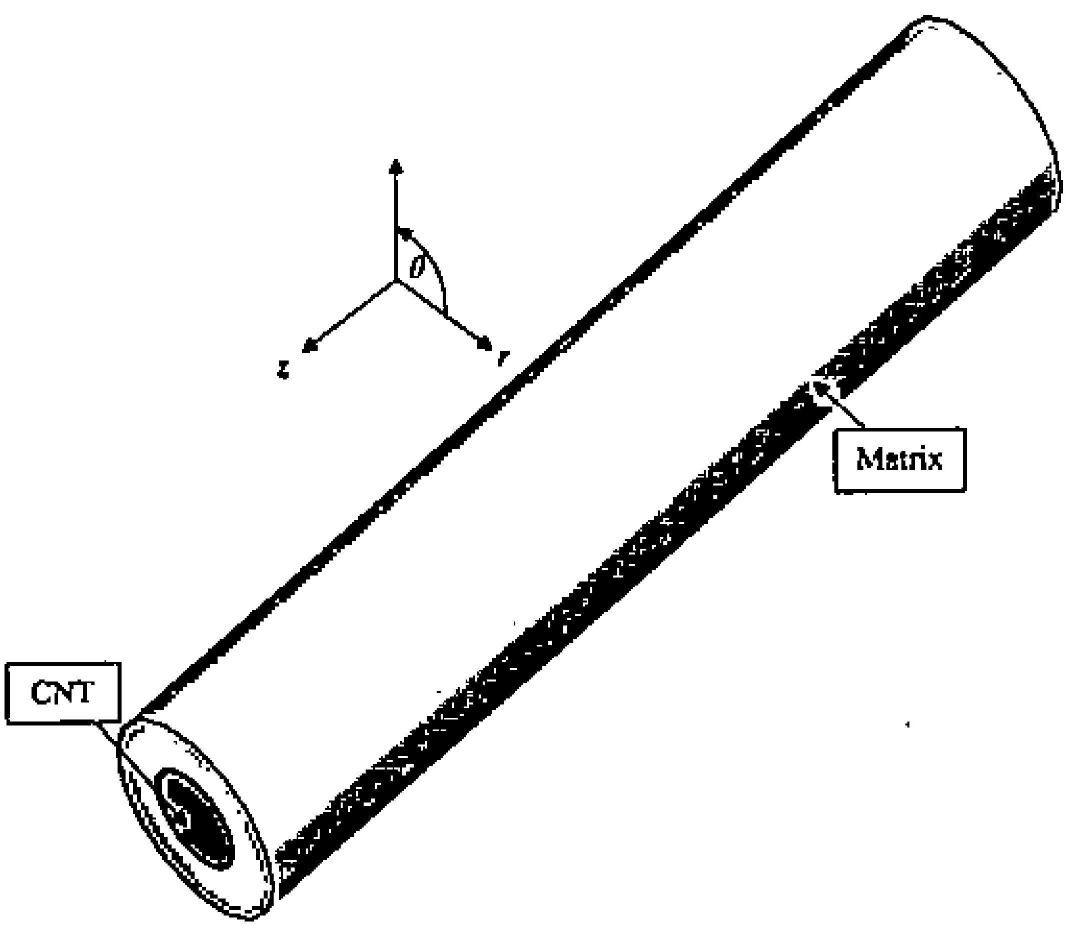

Figure 4.1: The cylindrical RVE with long CNT

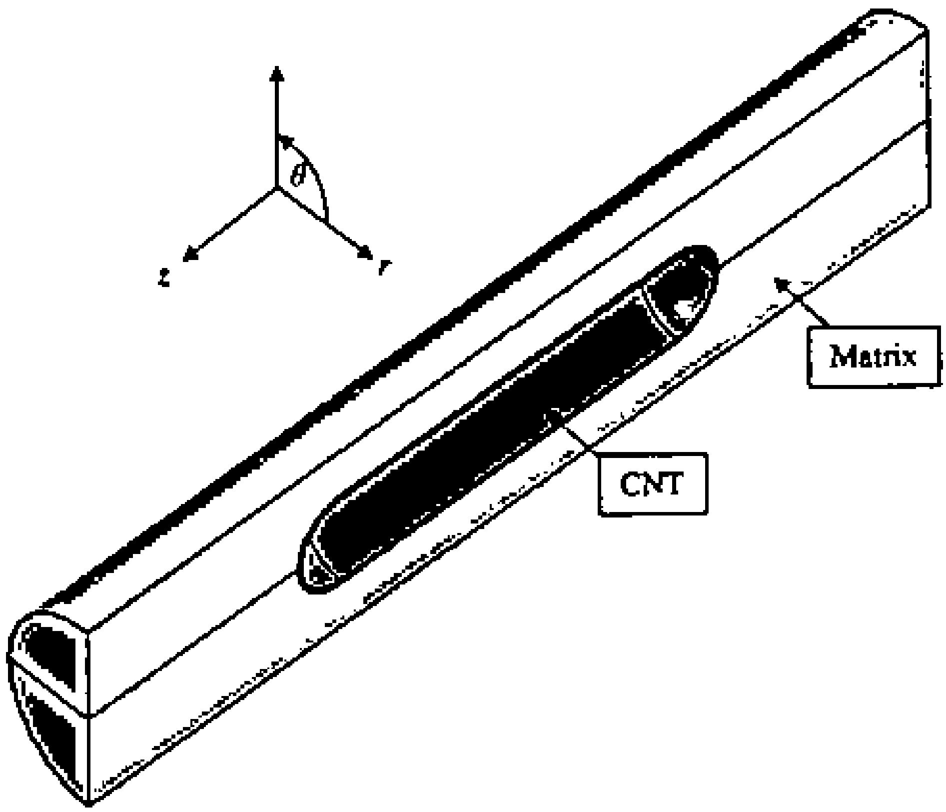

Figure 4.2: The cylindrical RVE with short CNT (cut-through view)

4.2 FORMULATION OF EQUATION USED TO DETERMINE THE EFFECTIVE YOUNG'S MODULUS

It is assumed that both the CNTs and matrix in a RVE are continua of linearly elastic, isotropic and homogenous materials, with given Young's moduli and Poisson's ratios. Under these assumptions, there will be two effective material constants to be determined for the CNT-based composite, namely, one Young's modulus E_z (= E_r) and one Poisson's ratio ν_{zr} (see Fig. 4.1 and 4.2 for the orientation of the coordinates). To derive the formula for extracting the TEM, an axi-symmetric elasticity model corresponding to the RVE is considered, as mentioned in chapter 3. Equation (3.2) states the axial strain, ε_z component which is expressed as,

$$\varepsilon_z = \frac{\sigma_z}{E} - \nu\frac{\sigma_r}{E} - \nu\frac{\sigma_\theta}{E} \tag{4.1}$$

The geometry of the elasticity model is corresponding to a hollow cylindrical RVE with length L, inner radius r_i and outer radius R, as shown in Fig. 4.3. This geometry can account for the cases when the CNT is relatively long and thus all the way through the length of the RVE. In the case that the CNT is relatively short and thus fully inside the RVE, a solid cylindrical RVE ($r_i = 0$) can be used for extracting the material constant, since the elasticity solutions are difficult to find in this case [21].

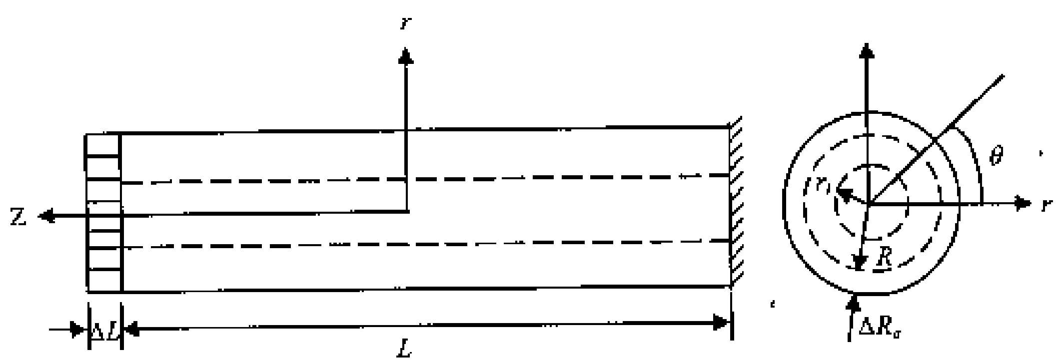

Figure 4.3: The cylindrical RVE used to evaluate the TEM of the CNT-based composites under axial stretch ΔL.

For the axial loading, shown in Fig. 4.3, the stress and strain components at any point on the lateral surface are,

$$\sigma_r = \sigma_\theta = 0,$$
$$\varepsilon_z = \frac{\Delta L}{L},$$
$$\varepsilon_\theta = \frac{\Delta R_a}{R},$$

with $\Delta R_a < 0$, if $\Delta L > 0$. Where ΔR_a is the radial displacement and r and θ indicate the radial and tangential components respectively. From Eq. (4.1), one has immediately,

$$E_z = \frac{\sigma_z}{\varepsilon_z} = \frac{L}{\Delta L}\sigma_{ave}, \tag{4.2}$$

where the averaged stress is given by [21],

$$\sigma_{ave} = \frac{1}{A}\int_A \sigma_z(x, y, L/2)dxdy, \tag{4.3}$$

with, A being the area of the end surface. σ_{ave} can be found for the RVE using the FEM results i.e. from the ANSYS 10.0 outputs.

Thus, to evaluate the effective Young's modulus of the CNT-based nanocomposites, the RVEs are studied using the finite element method first. Then the deformations and stresses are computed for the axial loading case (Fig. 4.3). After that, the FEM results are processed and Eq. (4.2) is applied to extract the effective Young's modulus for the CNT-based composites.

4.3 ANALYTICAL SOLUTION BASED ON THE STRENGTH OF MATERIALS THEORY

Some simple analytical expressions, or rules of mixtures, based on the strength of materials theory for estimating the effective Young's modulus E_z in the axial direction of the cylindrical RVEs are summarized in this section for the convenience of comparison. These expressions can be applied to validate the numerical results using the FEM and based on the elasticity formulas obtained in the previous section. Although the strength of materials theory is not accurate for stress, especially interfacial stress evaluations, it is fairly accurate and efficient in predicting the effective material constants in the axial direction of the RVEs, which are basically dependent on the overall responses of the RVEs [21].

4.3.1 RVE for long CNT

This is the case when the CNT is relatively long (with large aspect ratio) and therefore a segment can be modeled using an RVE.

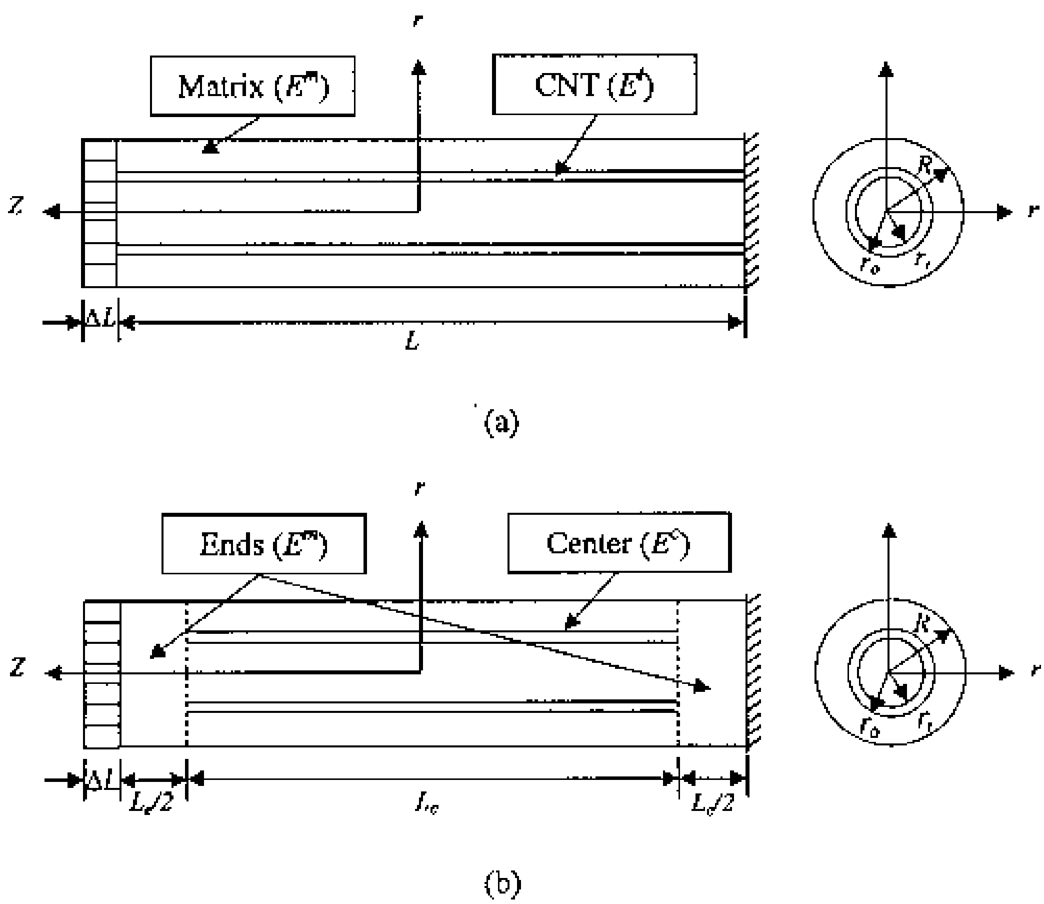

Figure 4.4: Simplified strength of materials models used to derive analytical expressions for the effective Young's modulus E_z, (a) CNT through the length of RVE, (b) CNT inside the RVE.

Here, the volume fraction of the CNT (a tube, Fig. 4.4(a)) is,

$$V^t = \frac{\pi(r_o^2 - r_i^2)}{\pi(R^2 - r_i^2)} = \frac{r_o^2 - r_i^2}{R^2 - r_i^2}. \tag{4.4}$$

Apply the strength of materials theory and assume the matrix and CNT deform independently of each other under the stretch ΔL (Fig. 4.4(a)). By considering the compatibility of strains and equilibrium of stresses, one obtains the following expression for the effective Young's modulus in the axial direction:

$$E_z = E^t V^t + E^m (1 - V^t), \tag{4.5}$$

where, E^m and E^t are the Young's modulus of the matrix and CNT, respectively. This is the same rule of mixtures as applied for predicting the effective Young's modulus in the fiber direction for conventional fiber-reinforced composites and is a close approximation of or identical (if the matrix and fiber have the same Poisson's ratio) to the elasticity solution [43, 44].

4.3.2 RVE for short CNT

In this case (Fig. 4.4(b)), the RVE can be divided into two segments: one segment accounting for the two ends with total length L_e and Young's modulus E^m and another segment accounting for the center part with length L_c and an effective Young's modulus E^c [21]. Note that the two hemispherical end caps of the CNT have been ignored in this derivation. Since the center part is a special case of Fig. 4.4(a), its effective Young's modulus is found to be

$$E^c = E^t V^t + E^m (1 - V^t). \tag{4.6}$$

Using Eq. (4.5), in which the volume fraction of the CNT, V^t, given by Eq. (4.4) is computed based on the center part of the RVE (with length L_c) only.

Again, by considering the compatibility of strains and equilibrium of stresses, one obtains the following expression for the effective Young's modulus in the axial direction [21]:

$$E_z = \left[\frac{1}{E^m}\left(\frac{L_e}{L}\right) + \frac{1}{E^c}\left(\frac{L_c}{L}\right)\left(\frac{A}{A_c}\right) \right]^{-1}. \tag{4.7}$$

Or in a more symmetric form:

$$\frac{1}{E_z} = \frac{1}{E^m}\left(\frac{L_e}{L}\right) + \frac{1}{E^c}\left(\frac{L_c}{L}\right)\left(\frac{A}{A_c}\right). \tag{4.8}$$

In which the areas $A = \pi R^2$ and $A_c = \pi\ (R^2 - r_i^2)$. Equation (4.7) or Eq. (4.8) can be viewed as an *extended rule of mixtures* compared to that given in Eq. (4.5), and can be employed to estimate the effective Young's modulus for the case shown in Fig. 4.4(b) when the CNT is inside the RVE. Equation (4.7) is also a more general result, as the result in Eq. (4.5) for the case of the RVE shown in Fig. 4.4(a) can be recovered from Eq. (4.7).

In the present study, Eqs. (4.5) and (4.7) are applied to verify the FEM estimates of the effective Young's modulus in the axial direction based on the elasticity results established in the previous section.

4.4 MODELING THE PROBLEM IN THE FINITE ELEMENT SOFTWARE

It is mentioned in chapter 3 that ANSYS 10.0 follows the same procedure as described in section 3.3.2. So, the modeling of the problems used in the current study also undergoes the pre-processing, solution and post-processing phases. The implementation of these phases for the present study is described below.

4.4.1 Pre-processing of the Models

The RVEs are analyzed using the commercial software ANSYS 10.0. In all cases, axi-symmetric FEM models are used since the RVEs have an axi-symmetric geometry and the loading case to be analyzed is axi-symmetric. The RVEs being axi-symmetric in nature, quadratic ring (or, axi-symmetric) elements are used for the study. Model size is minimized by invoking symmetry boundary conditions. As the models have symmetry about Z- axis, only one-half of the models are required to perform finite element analysis.

At the pre-processing stage in ANSYS 10.0, first the geometry of the models is drawn by generating the keypoints, lines and areas. Then it is meshed by a suitable element. In finite element method the mesh generation is the technique to subdivide a domain into a set of sub domains, called finite elements. The models, under investigation in the study, are meshed using PLANE 82 element, which is a quadratic (8-node) ring element. This element offer better accuracy for axi-symmetric model with axi-symmetric loading, which is described in chapter 3. Figure 4.5(a) and (b) show the view of two arbitrary models for long and short CNT cases respectively, after they are meshed.

4.4.2 Boundary Conditions and the Solution

After meshing of the models are completed, proper boundary conditions are applied to them. It is mentioned earlier that the models, used in the present study, are axi-symmetric in nature and for this reason, only one-half of them are analyzed. There are four sides of the 2D models. First two sides correspond to the ends of the models along the longitudinal axis and other two sides correspond to the transverse sides of the models, which are symmetric about the z-axis.

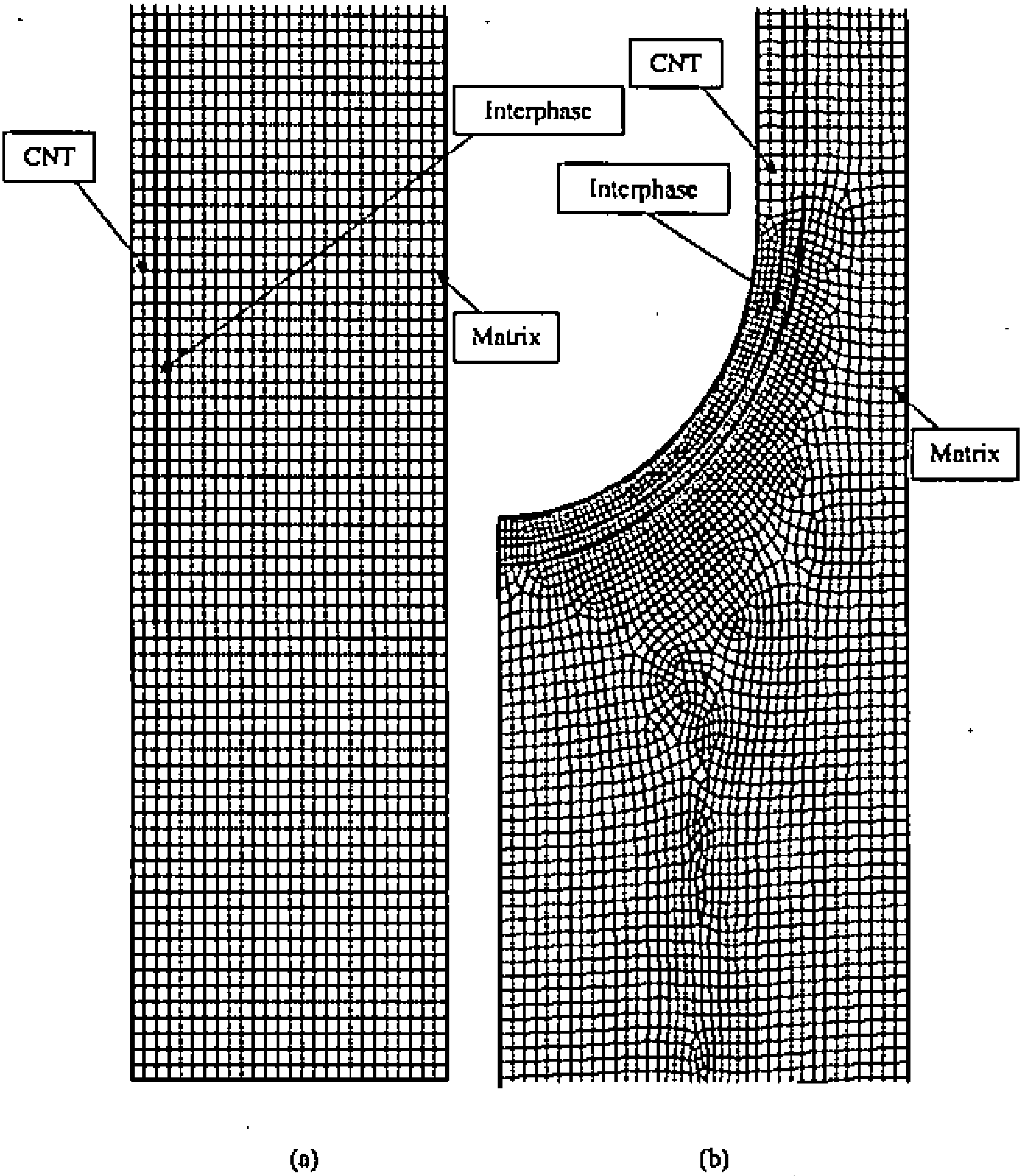

Figure 4.5: Partial view of the models after meshed (a) with long CNT; and (b) with short CNT.

Symmetry boundary conditions are applied to the symmetry sides. As the present study involves in the evaluation of the effective tensile elastic modulus, one end of models is made fixed and the other end is given displacement to a fixed value.

After applying the boundary conditions, the solution phases of the finite element analysis are executed. In this phase, computer takes over and solves the simultaneous equations that the finite element method generates. For the present study, the frontal solver is used for the solution of the finite element models.

4.4.3 Post processing

The general post processor contains the commands that allow displaying results of an analysis. All the vital information can be obtained by using the post processing command. In the present study, the quantity that is required is the 1st Principal stresses which are developed in the models due to the axial stretch. The 1st Principal stress distribution in the models can be obtained easily by the contour plot of these stresses. From the contour plot, the location where the maximum and minimum Principal stresses are concentrating can be easily observed. Again, after solution of a finite element analysis is made, the Principal stress at each nodal point can be obtained. The average values of these stresses are required to calculate the σ_{ave}, as required by Eq. (4.3). To calculate the effective tensile Young's modulus of the nanocomposites, the value of σ_{ave} is used that can be seen in Eq. (4.2).

CHAPTER 5
RESULTS AND DISCUSSION

In the preceding chapters, the computational techniques for determination of the effective tensile elastic modulus, determination of average stress, stress distribution in the finite element models have been presented. As mentioned earlier, two different types models are used, one of which is long and other one is short CNT embedded polymer composites, as shown in Fig. 4.1 and 4.2. One-half of the models are considered to analyze the study due to the axi-symmetry of them, as shown in Fig. 4.5.

For both type of models, four different investigations of effective tensile elastic modulus (TEM) are carried out. These are investigation of diameter effect of CNTs for perfect bonding between CNT and polymer matrix, examination of diameter effect of CNTs due to imperfect bonding between CNT and matrix, investigation of wall thickness effect of CNTs for perfect bonding and observation of interphase thickness effect due to imperfect bonding. The other two investigations are carried out only for the case of long CNT embedded composite. These are examination of waviness ratio effect of CNTs for a particular value of wavelength ratio and investigation of wavelength ratio effect of CNTs for different values of waviness ratio.

In the following sections, the results of all these investigations are shown graphically with detail description and also compared with analytical results.

5.1 EFFECT OF CNT DIAMETER ON THE TEM OF NANOCOMPOSITE FOR PERFECT BONDING

It is mentioned in chapter one, the nanotubes are of three different types based on chiral indices (m, n). They are Zigzag, Armchair and Criral type nanotubes. In the present research work, armchair type CNT is taken into consideration, which is specified by chiral indices (m, m). The radii of armchair CNTs are calculated using Eq. (1.3). To study the effect of CNT diameter variation on the effective tensile elastic modulus of polymer-based composite, the diameters of armchair tubules with the indices of (50, 50), (65, 65), (80, 80), (95, 95) and (110, 110) are considered, as shown in Table 5.1 sequentially. As mentioned earlier, both long and short CNT embedded in the polymer matrix are investigated. For both cases, the volume fraction of CNT in the composite is taken to be 5%.

To investigate the effect of diameter variation for long CNT, the cylindrical RVE, as shown in Fig. 4.1, is studied which shows the CNT all the way through its length. The length (L) of both matrix and CNT are 100 nm and the effective thickness (t) of CNT is taken as 0.4 nm. The radii (R) of matrix and the inner radii (r_i), outer radii (r_o) of CNTs for different values of CNT diameter of armchair tubules with above mentioned indices are given in Table 5.1.

Table 5.1: The radii of matrix and CNT for different values of CNT diameter for long CNT-based model

CNT diameter, D (nm)	Matrix radius, R (nm)	CNT inner radius, r_i (nm)	CNT outer radius, r_o (nm)
6.781	8.027	3.191	3.591
8.816	9.393	4.208	4.608
10.85	10.682	5.225	5.625
12.885	11.919	6.243	6.643
14.919	13.116	7.259	7.659

The Young's moduli and Poisson's ratios used for the CNT and matrix are:

CNT: $E^{f} = 1$ TPa, $\nu^{f} = 0.3$;
Matrix: $E^{m} = 5$ GPa, $\nu^{m} = 0.3$;

where, the value of the Young's modulus for the matrix is representative of a polymer.

It is already mentioned in section 4.4 that due to axi-symmetry of the model, only one-half of it is considered to perform the finite element analysis using finite element software ANSYS 10.0. The finite element mesh of one of the long RVEs with 10.85 nm of CNT diameter is shown in Fig. 5.1.

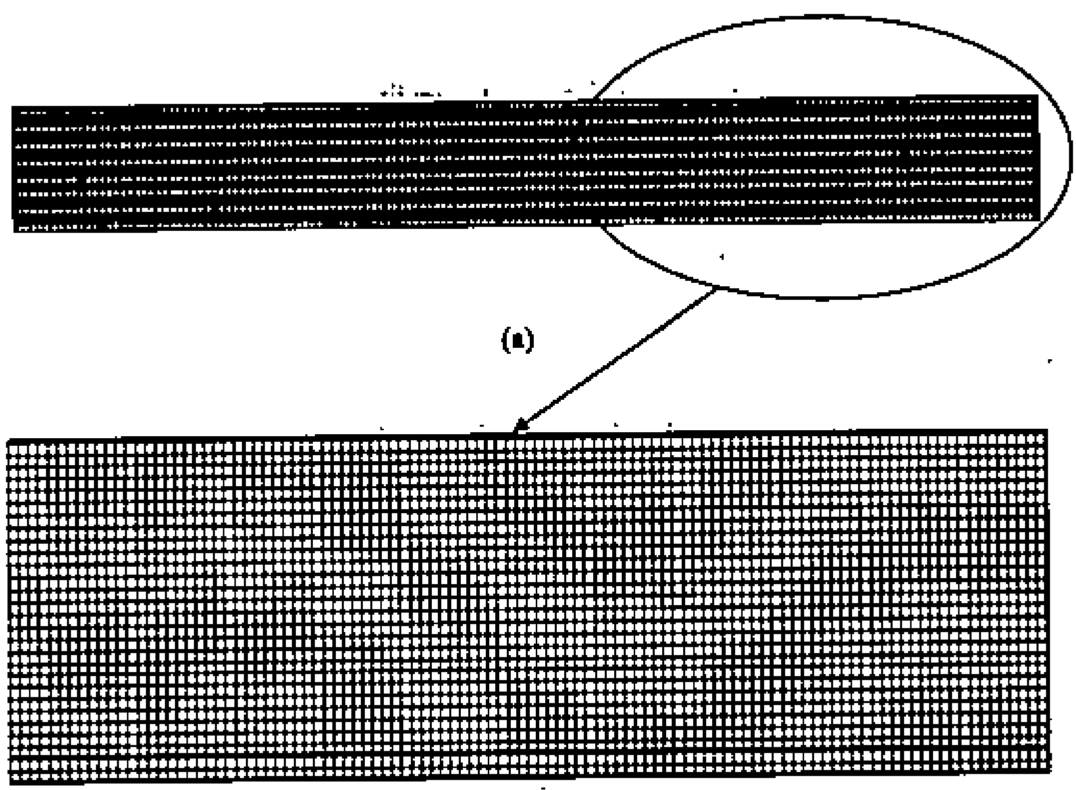

(a)

(b)

Figure 5.1: Axi-symmetric finite element mesh for the long CNT-based model with 10.85 nm of CNT diameter, (a) full view (b) partial enlarged view.

It is also mentioned in section 4.4, quadratic (8-node) ring elements are used to mesh the models throughout the study, which is called PLANE 82 element in ANSYS. All the FEM models are loaded axially, as shown in Fig. 4.3. The stress contour plot of the first principal stresses in the RVE with 10.85 nm of CNT diameter, under axial stretch is shown in Fig. 5.2.

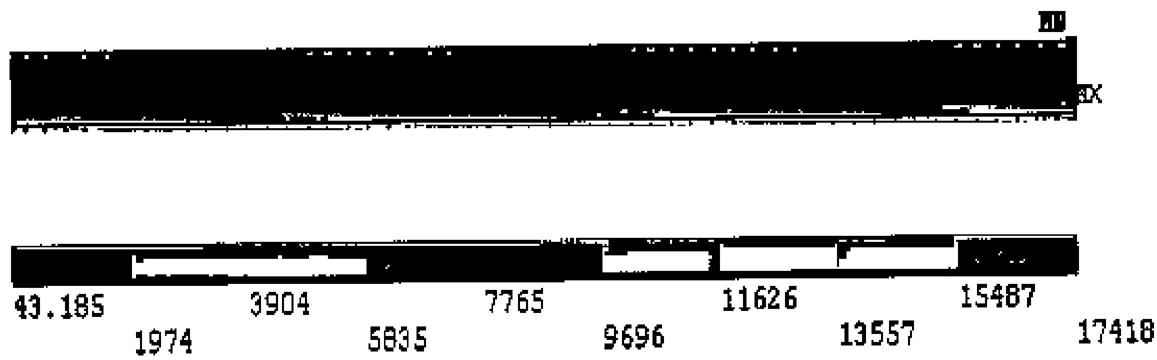

Figure 5.2: Plot of the first principal stresses for the long CNT-based model with 10.85 nm of CNT diameter under the axial stretch ($\Delta L = 1$ nm)

The effective tensile elastic modulus (TEM), E_z of the RVE is extracted from Eq. (4.2) using the FEM results. The FEM results for the CNT diameter variation on the effective TEM of the long CNT-based composite studied is shown in Fig. 5.3. The strength of materials solutions for the effective Young's modulus E_z, using Eq. (4.5), is also shown in Fig. 5.3 for comparison. The strength of materials solutions (Eq. (4.5)) are identical to those using the FEM, due to the simple geometry and load condition.

It is observed from Fig. 5.3 that the effective TEM of polymer-based composite increases with the increase in CNT diameter at a particular volume fraction of the CNT (5%) though the rate of increment is not rapid. This is due to the increased cross sectional area of the CNT, which allows the composite to take more loads in the axial direction. The results in Fig 5.3 also reveal that the increase of the stiffness of the composite is significant in the axial direction. With the volume fraction of the CNT being at only about 5%, the stiffness of the composite in the axial direction

(E_z) can increase by more than ten times compared with that of the polymer matrix, when $E^t / E^m = 200$.

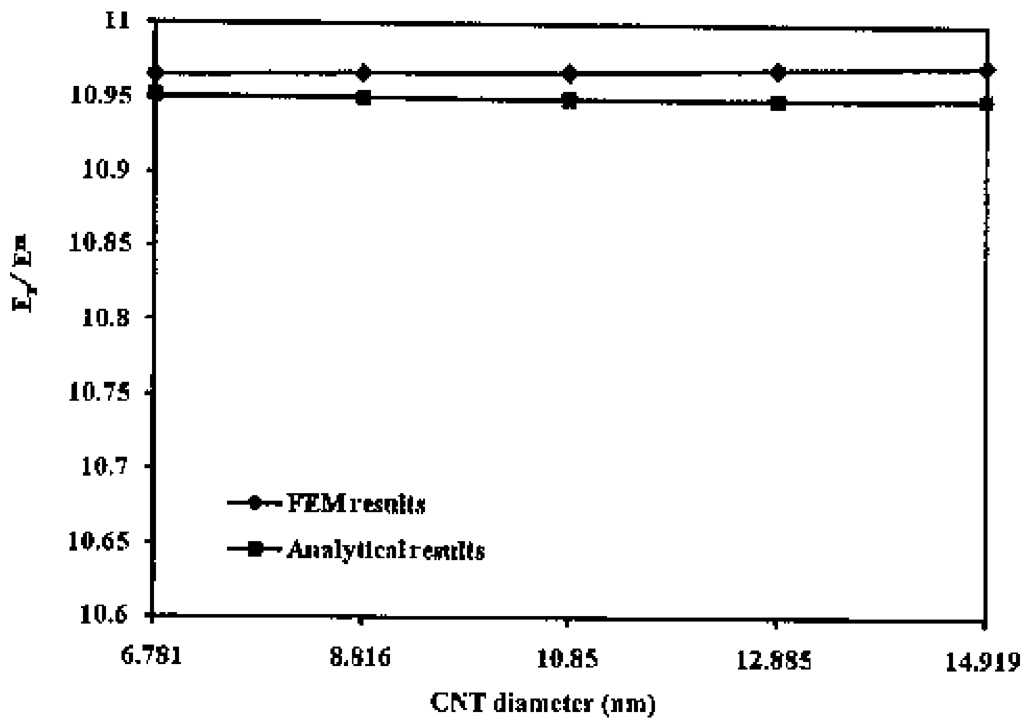

Figure 5.3: Effect of nanotube diameter variation on the TEM of nanocomposite for long CNT ($V_{CNT} = 5\%$).

Next, the RVE with a short CNT in the polymer matrix, as shown in Fig. 4.2, is studied to observe the effect of CNT diameter variation on the effective TEM of nanocomposite. The length (L) of the matrix is same as for the RVE with long CNT, except for the CNT total length, which is reduced to 50 nm (with the two hemispherical end caps). The radii (R) of matrix for different values of CNT diameter of armchair tubules with the same indices for 5% volume fraction of CNT are given in Table 5.2. Again, the thickness (t) of the CNT is considered same as for long CNT, *i.e.* 0.4nm.

Table 5.2: The radii of matrix for different values of CNT diameter for short CNT-based model

CNT diameter, D (nm)	Matrix radius, R (nm)
6.781	5.631
8.816	6.584
10.85	7.452
12.885	8.288
14.919	9.087

The Young's moduli and Poisson's ratios used for the CNT and matrix are same as the RVE with long CNT. The finite element mesh of one of the short RVEs with 10.85 nm of CNT diameter is shown in Fig. 5.4.

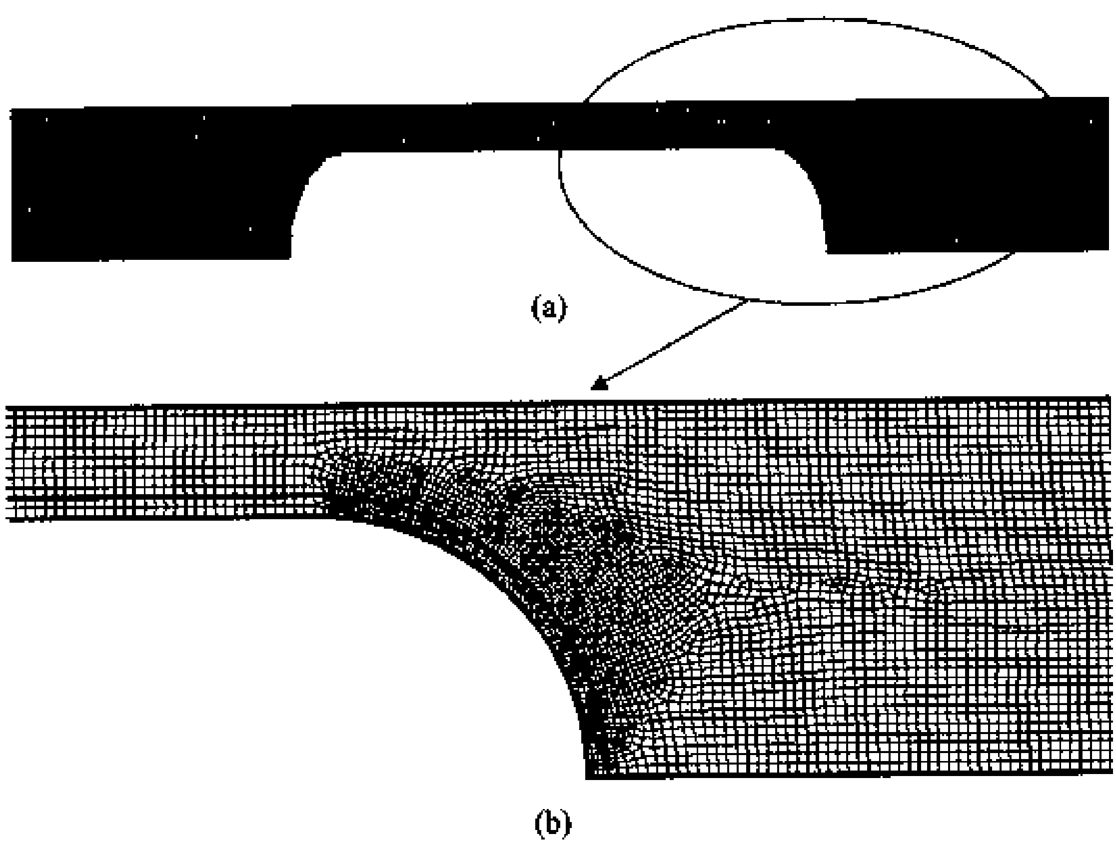

Figure 5.4: Axi-symmetric finite element mesh for the short CNT-based model with 10.85 nm of CNT diameter, (a) full view (b) partial enlarged view.

Again, the models with short CNT are meshed using the element PLANE 82. The stress contour plot of the first principal stresses in the RVE with 10.85 nm of CNT diameter, under axial stretch is shown in Fig. 5.5.

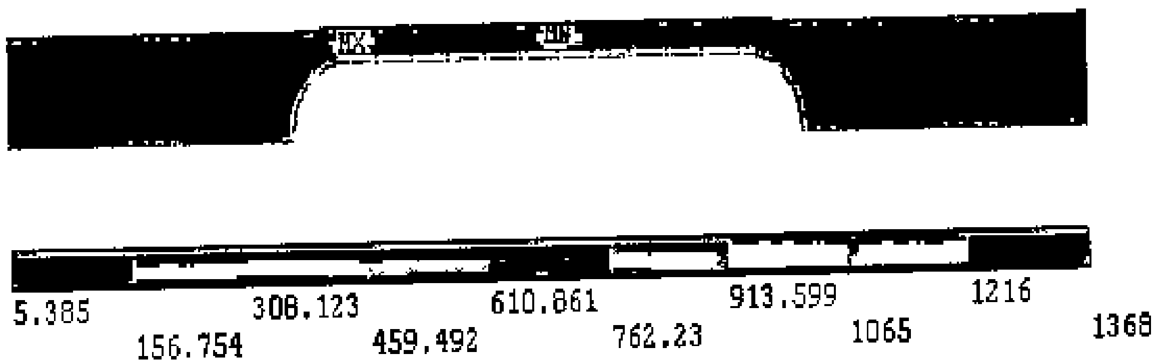

Figure 5.5: Plot of the first principal stresses for the short CNT-based model with 10.85 nm of CNT diameter under the axial stretch ($\Delta L = 1$ nm)

The FEM results for the CNT diameter variation on the effective TEM of the short CNT-based composite studied is shown in Fig. 5.6, along with the strength of materials solutions (Eq. (4.7)). The strength of materials solutions for the effective Young's modulus E_z, using the extended rule of mixtures, are quite close to the FEM solutions which are based on 3-D elasticity, with the difference less than 8%. Therefore, the extended rule of mixtures (Eq. (4.7)) may serve as a quick tool to estimate the stiffness of CNT-based composites in the axial direction when CNTs are relatively short, while the conventional rule of mixtures (Eq. (4.5)) can serve in cases when the CNTS are relatively long.

It can be seen from Fig. 5.6 that effective TEM of nanocomposite decreases with the increase in CNT diameter with a slow rate. Though the surface area of interface between CNT and matrix increases with the increase in CNT diameter, it results in larger end caps. These larger end cap areas take more transverse load than the smaller end caps though the load in the RVE is axial. This may lead to lower effective TEM of the composite with the increase in CNT diameter. Figure 5.6 also reveals that the increase of the stiffness in axial direction is moderate. It suggests that short CNTs in a matrix may not be as effective as long CNTs in reinforcing the composites.

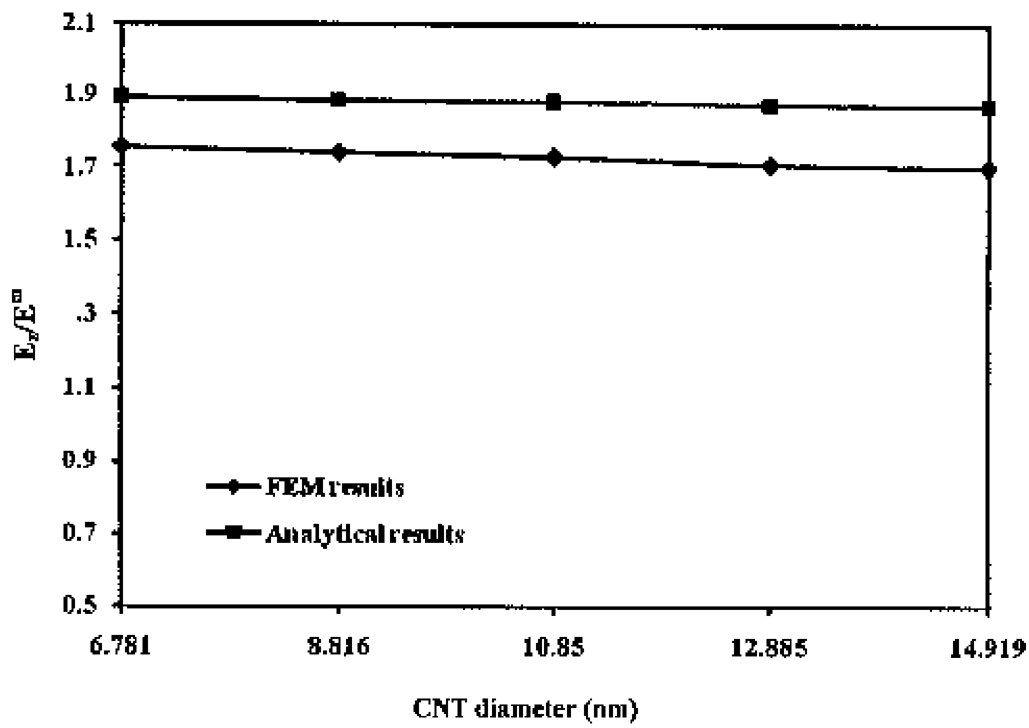

Figure 5.6: Effect of nanotube diameter variation on the TEM of nanocomposite for short CNT (V_{CNT} = 5%).

5.2 EFFECT OF CNT DIAMETER ON THE TEM OF NANOCOMPOSITE FOR IMPERFECT BONDING

It is already mentioned that an interphase is unavoidable in the production of polymer matrix composites and can form in a number of ways [22], for example:

- The presence of adsorbed contaminants on the fiber surface, which are not adsorbed during impregnation and cure;
- Diffusion of chemical species to the interface between fiber and matrix;
- Acceleration or retardation of polymerization at the interface;

- The deliberate inclusion of sizing resin at the time of fiber manufacture.

The effect of an interphase on the performance of composite is not well characterized, since its precise nature is difficult to predict [49]. Both Scanning Force microscopy (SFM) [50] and Scanning probe microscopy (SPM) have been used to examine the mechanical and thermal properties in the immediate vicinity of reinforcing fibers [51, 52]. In this way, it has been clearly shown that sized reinforcing fibers modify the properties of the matrix over a region of around 0.5 μm. It is also found experimentally that an interphase can be both soft and stiff compared to the matrix [49].

Here, an interphase of 0.2 nm thickness is considered between CNT and matrix to examine the effect of CNT diameter variation on the TEM of polymer composites in the presence of both soft and stiff interphases. Both long and short CNT models are examined to observe this effect.

For long CNT-based model, the dimensions of matrix and CNT are same as the dimensions mentioned in Table 5.1, with the addition of 0.2 nm thick interphase between CNT and matrix. The Young's moduli and Poisson's ratios used for matrix and CNT are same as considered in the section 5.1. The Young's modulus and Poisson's ratio of interphase are as follows:

Interphase: $E^i = 7$ GPa (Stiff) and 3 GPa (Soft), $\nu^i = 0.3$

The partial view of the finite element mesh of one of the long RVEs with 10.85 nm of CNT diameter along with 0.2 nm thick interphase has been shown in Fig. 5.7.

Again, the stress contour plot of the first principal stresses in the RVE with 10.85 nm of CNT diameter along with 0.2 nm thick interphase, under axial stretch is shown in Fig. 5.8.

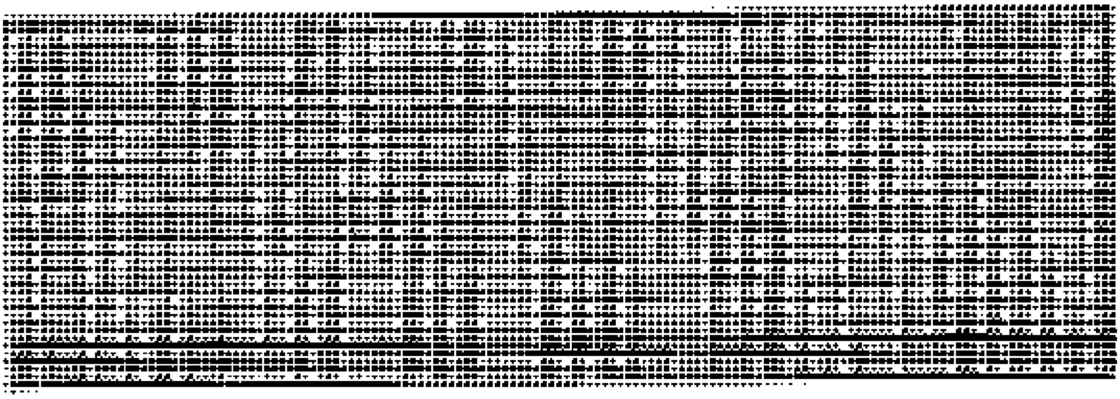

Figure 5.7: Partial view of the finite element mesh of the long CNT-based model for imperfect bonding.

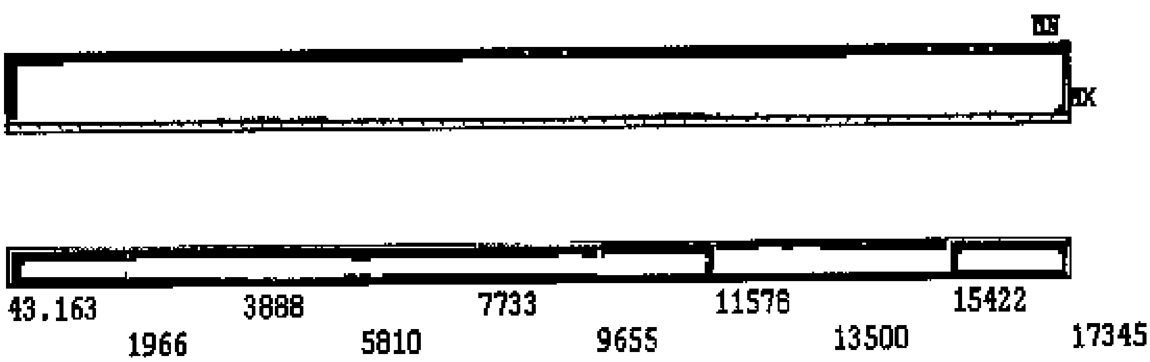

Figure 5.8: Plot of the first principal stresses for the RVE (long CNT) with 0.2 nm thick interphase under axial stretch ($\Delta L = 1$ nm).

The FEM results for the CNT diameter variation on the effective TEM of the long CNT-based composite, with 0.2 nm thick interphase, studied is shown in Fig. 5.9. It shows the TEM for both soft and stiff interphase along with the result of perfect bonding for comparison.

It is seen that change in CNT diameter at the presence of interphase has the same effect as for perfect bonding on the TEM of nanocomposite. That is, effective TEM increases with the increase of CNT diameter for long CNT. It is also observed that the value of effective TEM for stiff interphase is higher than perfect bonding at a particular CNT diameter. On the contrary, this value is lower than perfect bonding for soft interphase. It should be mentioned that the presence of interphase may increase brittleness in the composite structure.

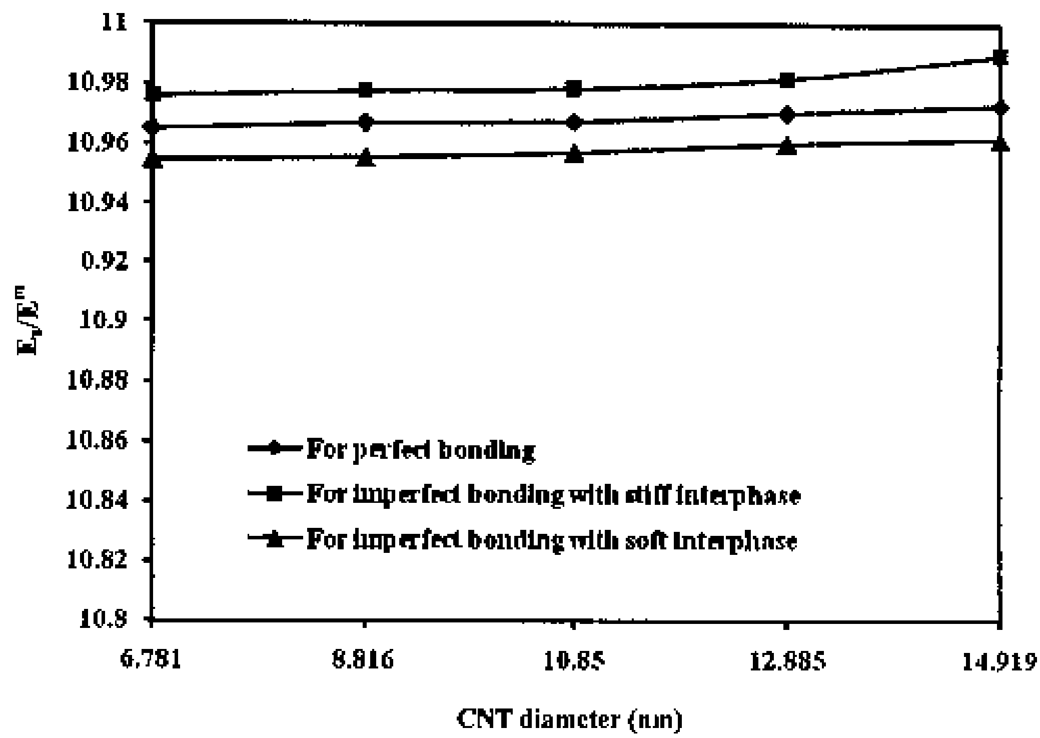

Figure 5.9: Effect of nanotube diameter variation on the TEM of nanocomposite with long CNT for imperfect bonding (V_{CNT} = 5%).

Next, for short CNT with interphase thickness of 0.2 nm, the dimensions of matrix and CNT are same as the dimensions mentioned in Table 5.2. The Young's moduli and Poisson's ratios used for matrix and CNT are same as considered in section 5.1. The Young's modulus and Poisson's ratio of interphase are same as for long CNT-based model, given by,

Interphase: E^i = 7 GPa (Stiff) and 3 GPa (Soft), $\nu^i = 0.3$

The partial view of the finite element mesh of one of the short RVEs with 10.85 nm of CNT diameter along with 0.2 nm thick interphase is shown in Fig. 5.10.

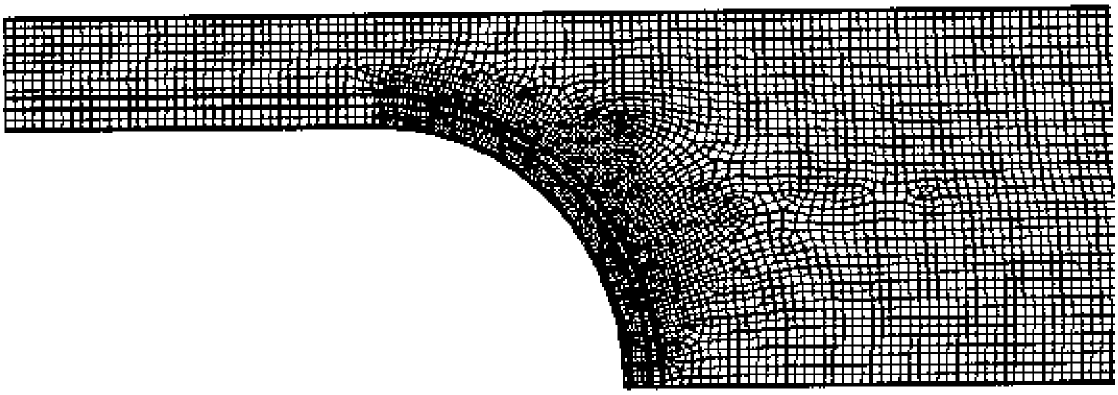

Figure 5.10. Partial view of the finite element mesh of the short CNT-based model for imperfect bonding.

The stress contour plot of the first principal stresses in the RVE with 10.85 nm of CNT diameter with 0.2 nm thick interphase, under axial stretch is shown in Fig. 5.11.

Again, The FEM results for the CNT diameter variation on the effective TEM of the short CNT-based composite, with 0.2 nm thick interphase, studied is shown in Fig. 5.12. It shows the TEM for both soft and stiff interphase along with the results of perfect bonding for comparison

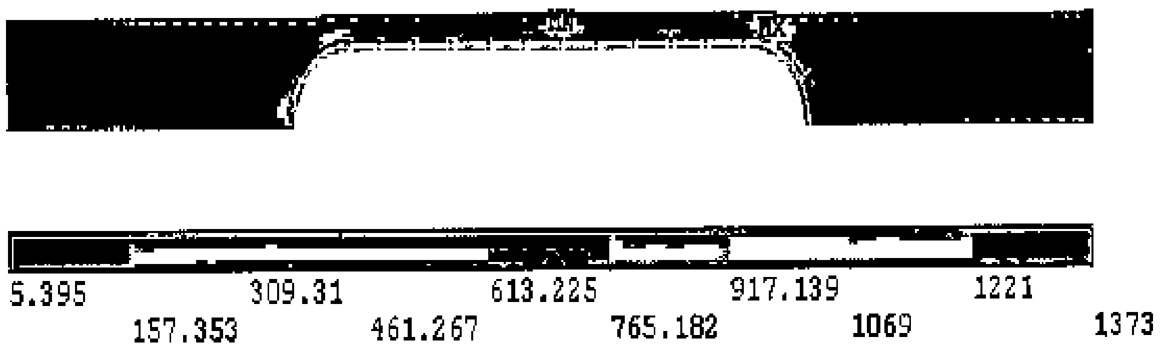

Figure 5.11: Plot of the first principal stresses for the RVE (short CNT) with 0.2 nm thick interphase under axial stretch (ΔL = 1 nm).

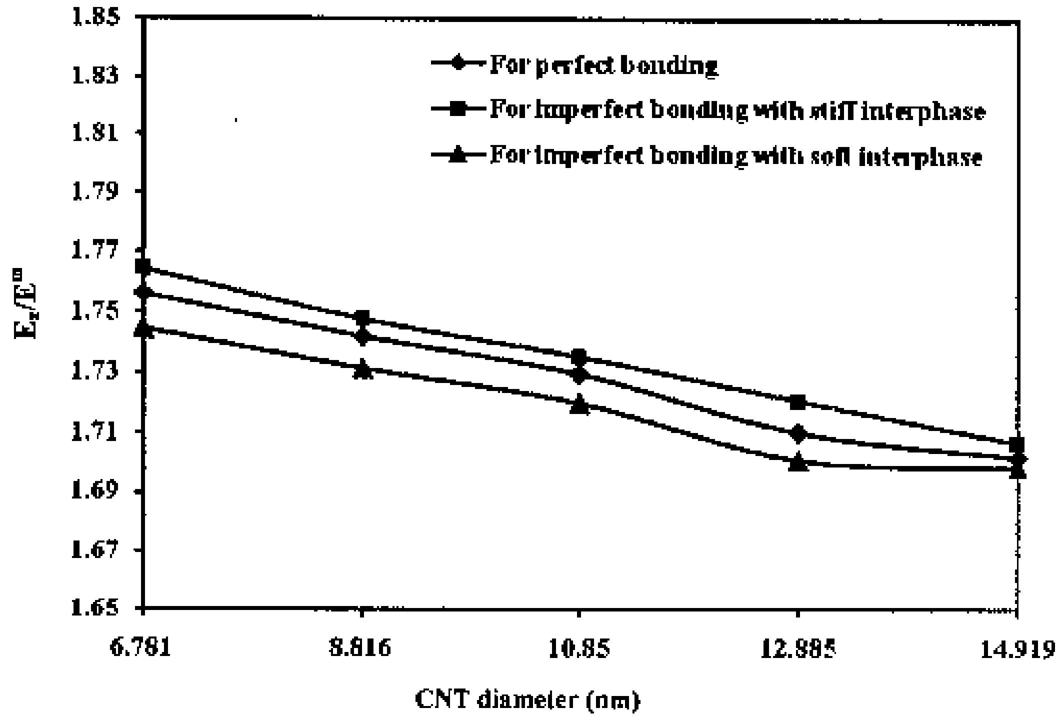

Figure 5.12: Effect of nanotube diameter variation on the TEM of nanocomposite for short CNT with imperfect bonding (V_{CNT} = 5%).

It is seen that change in CNT diameter at the presence of interphase has the same effect as for perfect bonding on the TEM of nanocomposite. That is, effective tensile elastic modulus decreases with the increase of CNT diameter for short CNT. It is also observed that at a particular CNT diameter, the value of effective TEM for stiff interphase is higher than perfect bonding, while this value is lower than perfect bonding for soft interphase. This effect is same as long CNT-based composite.

5.3 EFFECT OF INTERPHASE THICHNESS ON THE TEM OF NANOCOMPOSITE

Some experimental works have shown that interphase thickness can vary from one composite to other due to several reasons, such as presence of adsorbed contaminants on the fiber surface, diffusion of chemical species at the interface, acceleration or retardation of polymerization at the interface between fiber and matrix, etc. [49, 53]. In this section, effect of interphase thickness variation is examined on the effective TEM of composite for both stiff and soft interphase cases. Both long and short CNT models are considered for investigation. The interphase thicknesses are taken to be 0.2, 0.6, 1.0 and 1.5 nm based on an experimental work [49].

For long CNT model, the dimensions of matrix and CNT are taken from Table 5.1. The Young's moduli and Poisson's ratios of matrix, interphase and CNT are considered same as section 5.2.

The partial view of the finite element mesh of one of the long RVEs with 10.85 nm of CNT diameter along with 0.6 nm thick interphase is shown in Fig. 5.13.

Figure 5.13: Partial view of the finite element mesh of the long CNT-based model with 0.6 nm thick interphase.

Again, the stress contour plot of the first principal stresses in the RVE with the CNT indices of (80, 80) and interphase thickness of 0.6 nm, under axial stretch is shown in Fig. 5.14.

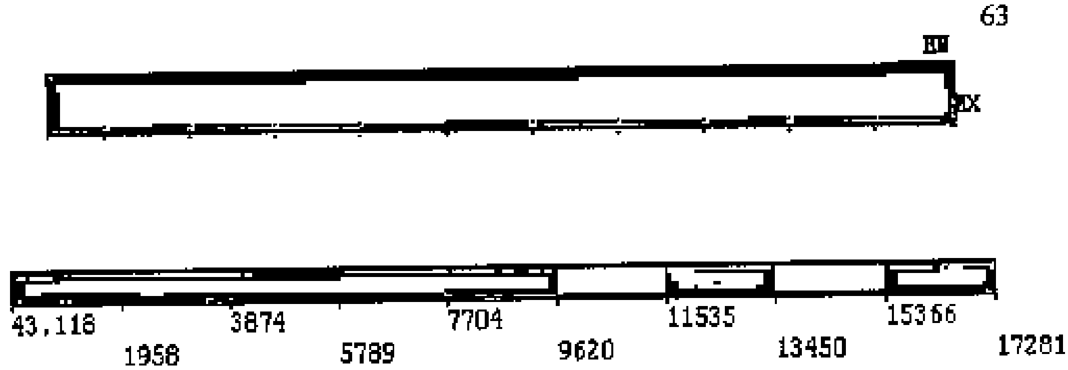

Figure 5.14: Plot of the first principal stresses for the RVE (long CNT) with 0.6 nm thick interphase under axial stretch (ΔL = 1 nm).

The FEM results for the interphase thickness variation on the effective TEM of the long CNT-based composite studied is shown in Fig. 5.15. It shows the TEM for both soft and stiff interphase along with the results of perfect bonding (i.e. no interphase) for comparison.

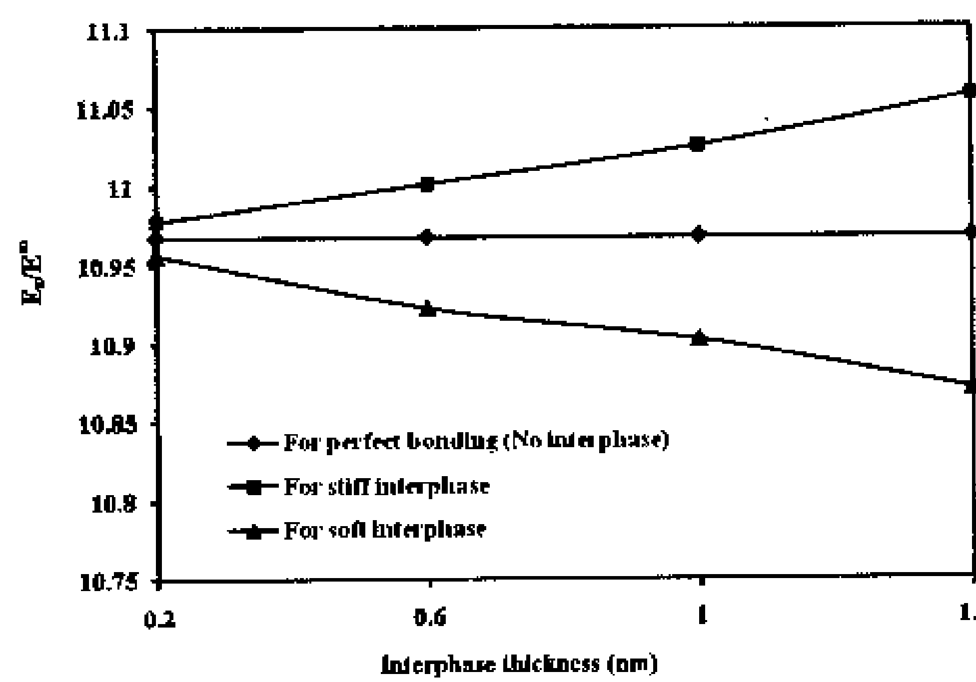

Figure 5.15: Effect of interphase thickness variation on the TEM of nanocomposite for long CNT (V_{CNT} = 5%).

It is clear from Fig. 5.15 that effective TEM of composite increases gradually with the increase in interphase thickness for stiff interphase, while it decreases gradually in case of soft interphase. As there is no interphase for perfect bonding, this value remains constant throughout.

Next, for short CNT model, the dimensions of matrix and CNT are same as the dimensions mentioned in Table 5.2, with various interphase thicknesses, mentioned above, between CNT and matrix. The properties of matrix, interphase and CNT are same as for long CNT model.

The partial view of the finite element mesh of one of the short RVEs with 10.85 nm of CNT diameter along with 0.6 nm thick interphase is shown in Fig. 5.16.

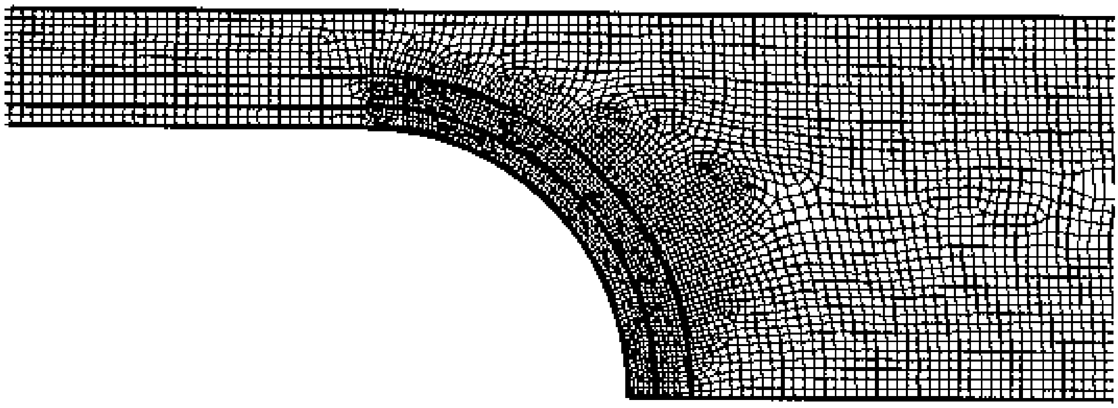

Figure 5.16: Partial view of the finite element mesh of the short CNT-based model with 0.6 nm thick interphase.

Again, the stress contour plot of the first principal stresses in the RVE with the CNT indices of (80, 80) and interphase thickness of 0.6 nm, under axial stretch is shown in Fig. 5.17.

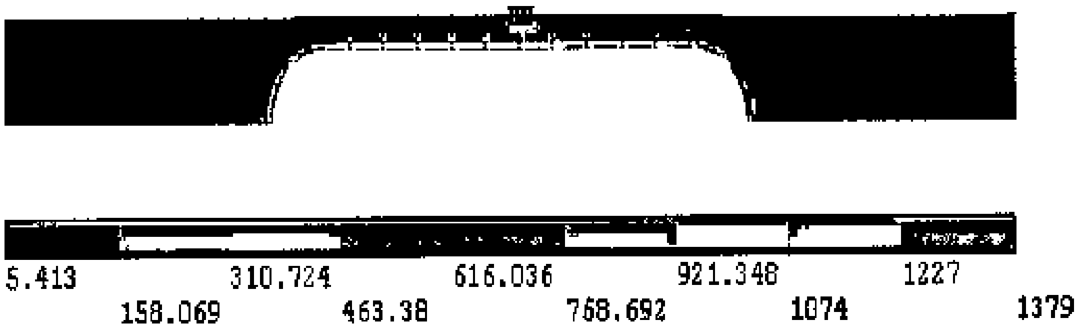

Figure 5.17: Plot of the first principal stresses for the RVE (short CNT) with 0.6 nm thick interphase under axial stretch ($\Delta L = 1$ nm).

The FEM results for the interphase thickness variation on the effective TEM of the short CNT-based composite studied is shown in Fig. 5.18. It also shows the TEM for both soft and stiff interphase along with the results of perfect bonding (i.e. no interphase) for comparison.

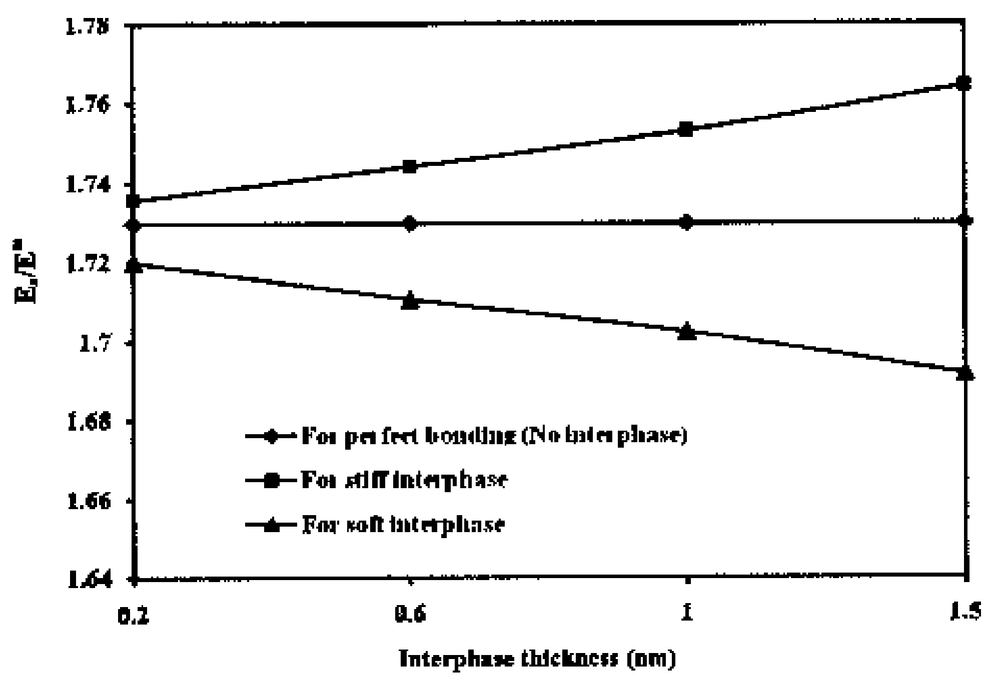

Figure 5.18: Effect of interphase thickness variation on the TEM of nanocomposite for short CNT ($V_{CNT} = 5\%$).

It is observed from Fig. 5.18 that effective TEM of short CNT-based composite increases gradually with the increase in interphase thickness for stiff interphase, while it decreases gradually in case of soft interphase. This behavior is exactly same as long CNT-based model. It can be mentioned that larger interphase thickness changes the characteristics of CNT-based polymer composite significantly which is not desirable. It requires great emphasize to minimize the presence of interphase during fabrication of CNT-based polymer composites.

5.4 EFFECT OF CNT WALL THICKNESS ON THE TEM OF NANOCOMPOSITE FOR PERFECT BONDING

It is mentioned in chapter one, CNTs can be broadly classified into three categories: single-walled nanotubes (SWNT), multi-walled nanotubes (MWNT) and nanotube bundles or ropes. In MWNTs, a number of concentric SWNTs held together with relatively weak van der Waals forces. For MWNTs, inter-layer sliding (so-called "sword and sheath" slippage [54]) could limit their potential as structural reinforcement. On the contrary, some researchers have found evidence of promising MWNT-polymer interactions in composite materials [16, 55].

In the present study, the effect of CNT layer variation of MWNTs on effective TEM of composite is investigated. Here, an assumption is made in modeling the problem. That is, by modeling the nanotube as a continuum we are disregarding the specific form of the MWNT and neglecting any possible relative motion between individual CNTs in a MWNT. This assumption suggests that effective TEM as calculated here is an "upper bound" for the given model, in that modeling sliding of the tubes or shells would further reduce the effective Young's modulus of nanotubes. By this assumption, we are actually varying the wall thicknesses of SWNTs. Here, the thicknesses are varied from one to five layers to investigate the effect on TEM of composite. Both long and short CNT-based models are considered for the CNT with indices (95, 95). The outer diameter of CNT with indices (95, 95) is kept fixed and inner diameter is changed by considering the thickness of one single layer as 0.4 nm. In this way, the layers of MWNTs are incorporated.

For long CNT-based model, the length (L) of the RVE is considered same as previous models. The radii (R) of matrix and the inner radii (r_i), outer radii (r_o) of CNTs for different values of CNT thicknesses are given in Table 5.3. The Young's moduli and Poisson's ratios used for the CNT and matrix are same as considered in section 5.1.

Table 5.3: The radii of matrix and CNT for different values of CNT wall thicknesses for long CNT-based model

CNT thickness, t (nm)	Matrix radius, R (nm)	CNT inner radius, r_i (nm)	CNT outer radius, r_o (nm)
0.4	11.919	6.243	6.643
0.8	15.294	5.843	6.643
1.2	17.880	5.443	6.643
1.6	19.985	5.043	6.643
2	21.749	4.643	6.643

The partial view of the finite element mesh of one of the long RVEs with 1.2 nm of CNT wall thickness is shown in Fig. 5.19.

Again, the stress contour plot of the first principal stresses in the RVE with 1.2 nm of CNT wall thickness for long CNT, under axial stretch is shown in Fig. 5.20.

Next, for short CNT-based model, the length (L) of the RVE is considered same as previous models. The radii (R) of matrix and for different values of CNT wall thicknesses are given in Table 5.4. The Young's moduli and Poisson's ratios used for the CNT and matrix are same as considered in section 5.1.

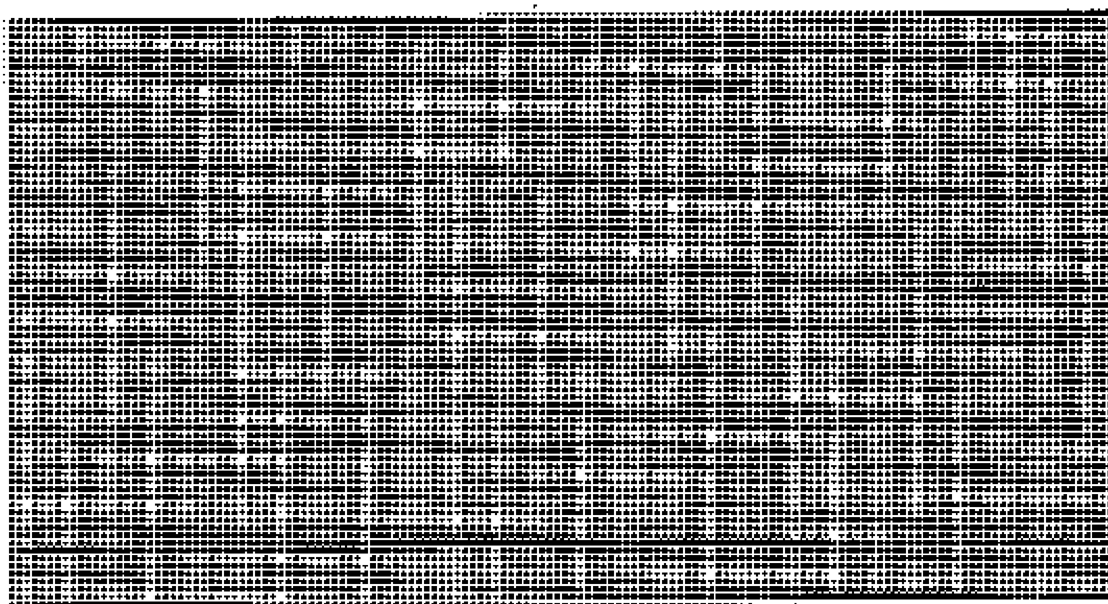

Figure 5.19: Partial view of the finite element mesh for the long CNT-based model with 1.2 nm of CNT wall thickness.

Figure 5.20: Plot of the first principal stresses for the RVE (long CNT) with 1.2 nm of CNT wall thickness under axial stretch ($\Delta L = 1$ nm).

The partial view of the finite element mesh of one of the short RVEs with 1.2 nm of CNT wall thickness is shown in Fig. 5.21.

Table 5.4: The radii of matrix for different values of CNT wall thicknesses for short CNT-based model

CNT thickness, t (nm)	Matrix radius, R (nm)
0.4	8.288
0.8	10.654
1.2	12.438
1.6	13.868
2	15.049

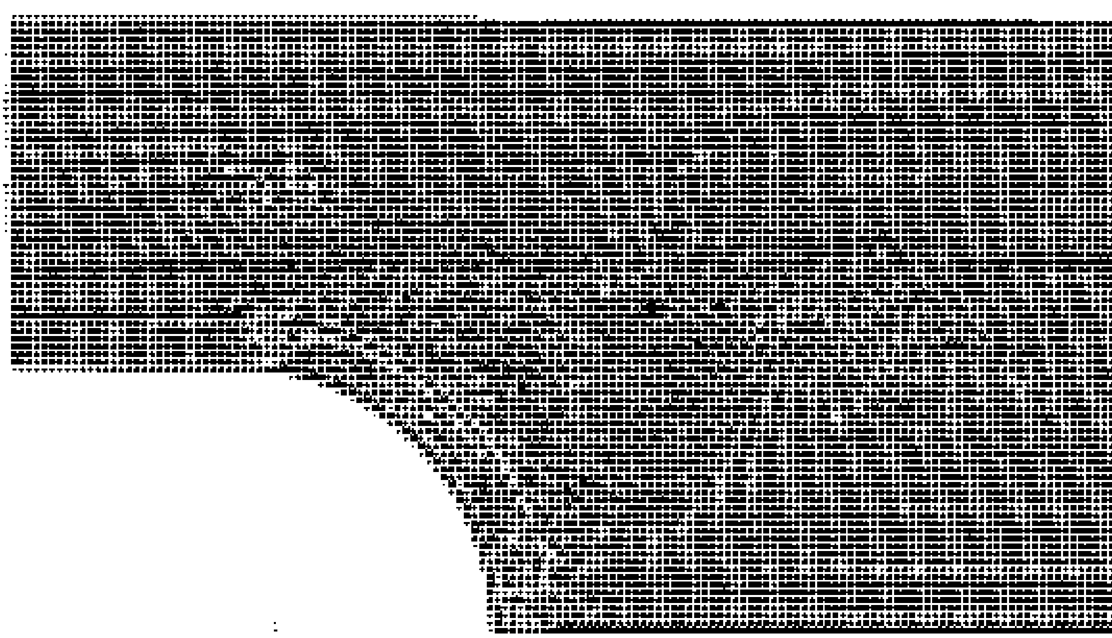

Figure 5.21: Partial view of the finite element mesh of the short CNT-based model with 1.2 nm of CNT wall thickness.

The stress contour plot of the first principal stresses in the RVE with 1.2 nm of CNT wall thickness for short CNT, under axial stretch is shown in Fig. 5.22.

Also, the FEM results for the CNT wall thickness variation on the effective TEM of both long and short CNT-based composite studied is shown in Fig. 5.23. Both FEM results are for perfect bonding between CNT and matrix.

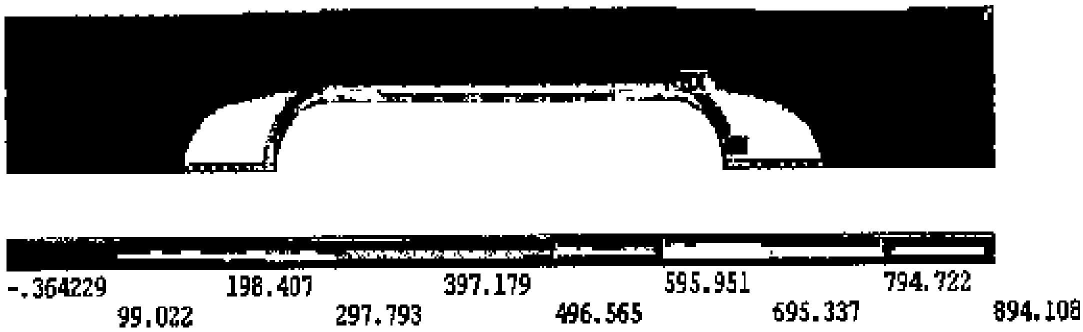

Figure 5.22: Plot of the first principal stresses for the RVE (short CNT) with 1.2 nm of CNT wall thickness under axial stretch (ΔL = 1 nm).

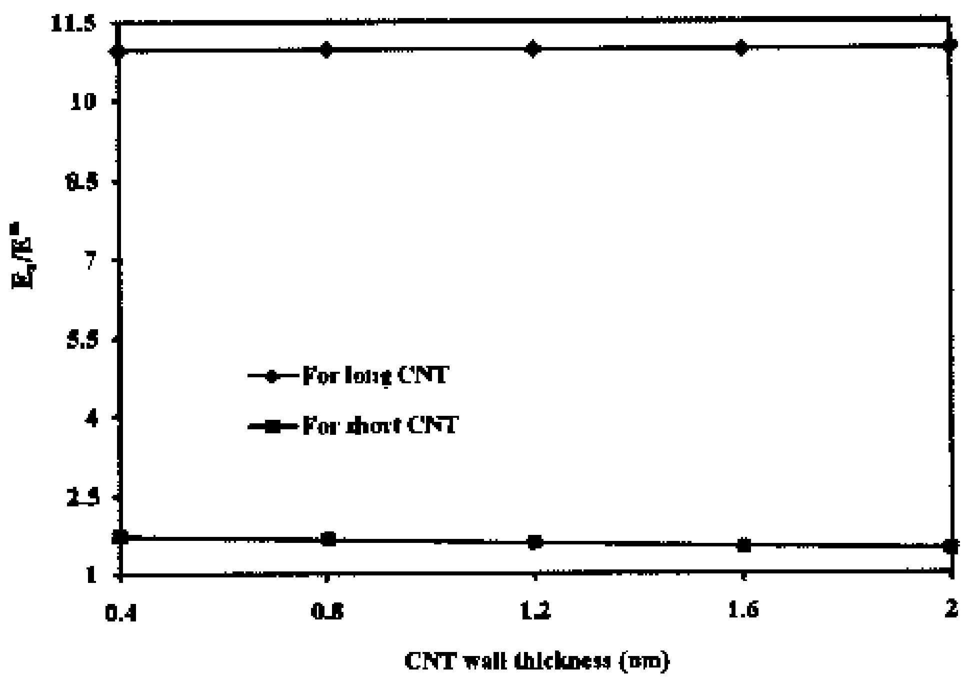

Figure 5.23: Effect of CNT wall thickness variation on the TEM of nanocomposite (V_{CNT} = 5%).

It is seen that effective TEM increases with increase in CNT wall thickness (i.e. increasing the layers of MWNTs) for long CNT. In contrast, effective TEM decreases with the increase in CNT wall thickness (i.e. increasing the layers of MWNTs) for short CNT. The reasons for these effects can be explained as follows. For long CNT-based model, the CNTs are carrying loads directly and as the thickness of CNTs increases, more loads can be carried by CNTs though the outer surface area of CNTs at the interphase is fixed. Again, for short CNT-based model, CNTs are not carrying the loads directly. These are contributing the composite only through interfacial load (stress) transfer. Though the CNT wall thickness is increasing, it is not increasing the surface area of the CNTs. At the same time, matrix radius is increasing with the increase in CNT wall thickness to maintain fixed volume fraction and more loads are carried by matrix. For this, effective TEM decreases with the increase in CNT wall thickness in case of short CNT.

5.5 EFFECT OF CNT WAVINESS ON THE TEM OF NANOCOMPOSITE

The issues identified before indicate several key aspects that influence the potential of CNTs reinforced in a polymer matrix. In all the above cases, CNTs are assumed to be straight in the polymer matrix. One issue which has not typically been associated with the modeling of CNT reinforced polymer composites but which seems critical based on micrograph images of these materials, is the characteristics waviness or curvature of embedded nanotubes [56]. Some other experimental works have shown the evidence that the embedded nanotubes in polymer matrix are not straight but rather have significant curvature or waviness that varies throughout the composite [16, 57].

In this section, the effect of nanotube waviness on the effective TEM of composite is examined. To determine the effective tensile modulus of an embedded wavy nanotube, finite element model is created for a single, infinitely long wavy nanotube of diameter d embedded in the matrix material. Nanotube waviness is modeled by prescribing a sinusoidal CNT shape of the form, $r = a\cos(2\pi z/\lambda)$. where, a and λ are the amplitude and wavelength of the nanotube respectively and z is the fiber axial direction. The waviness ratio (w) and wavelength ratio of the CNT are defined as (a/λ) and (λ/d) respectively. In the present study, the models are created with a fixed wavelength (λ), which is 200 nm. The amplitudes (a) are taken to be 2, 2.5, 3, 3.5 and 4 nm. The FE model is created with a wavelength of ($\lambda/2$ = 100 nm) and the CNT diameter is considered fixed, as 14.919 nm. The Young's moduli and Poisson's ratios used for the CNT and matrix are same as considered in section 5.1. Both perfect and imperfect bonding between CNT and matrix are modeled. Again, both stiff and soft interphases are considered. Their Young's modulus and Poisson's ratio are considered same as considered in section 5.2.

The finite element mesh of one of the long RVEs with 3 nm amplitude of sinusoidal CNT for perfect bonding is shown in Fig. 5.24.

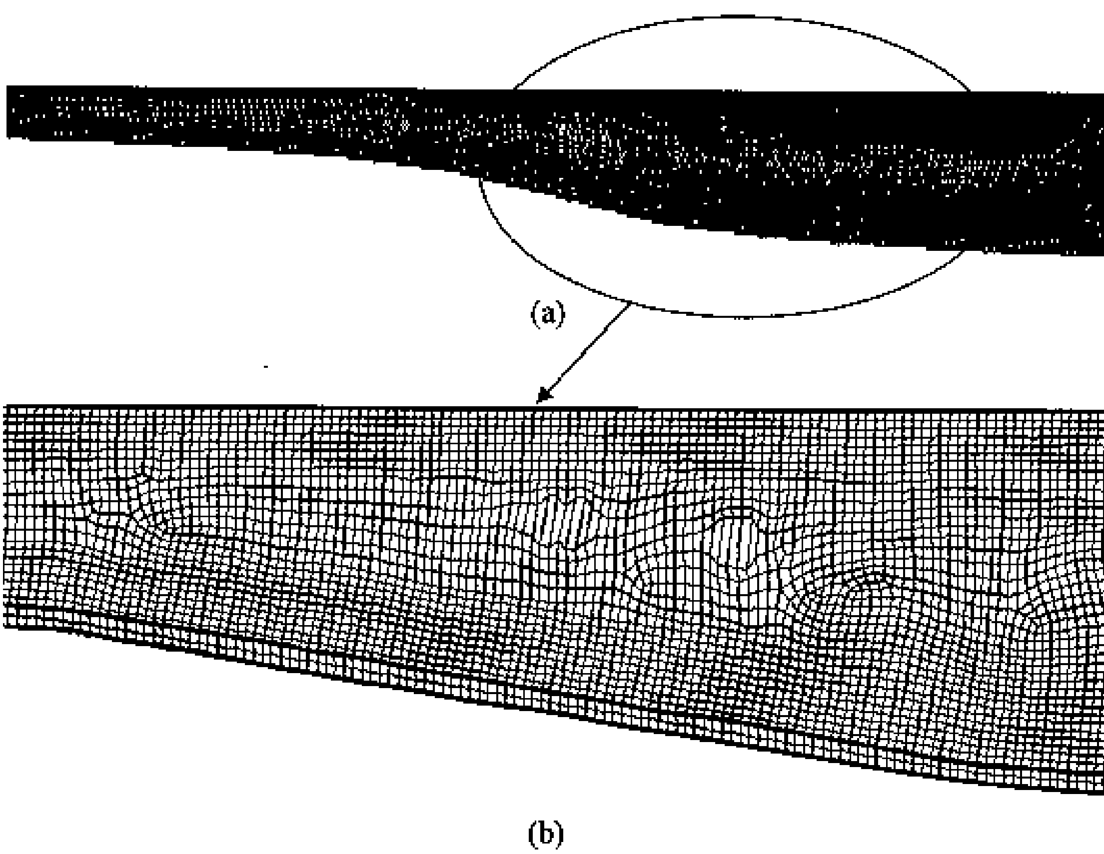

Figure 5.24: Finite element mesh of the model with 3 nm amplitude of sinusoidal CNT for perfect bonding, (a) full view (b) partial enlarged view.

The stress contour plot of the first principal stresses in the RVE with 3 nm amplitude of sinusoidal CNT for perfect bonding, under axial stretch is shown in Fig. 5.25.

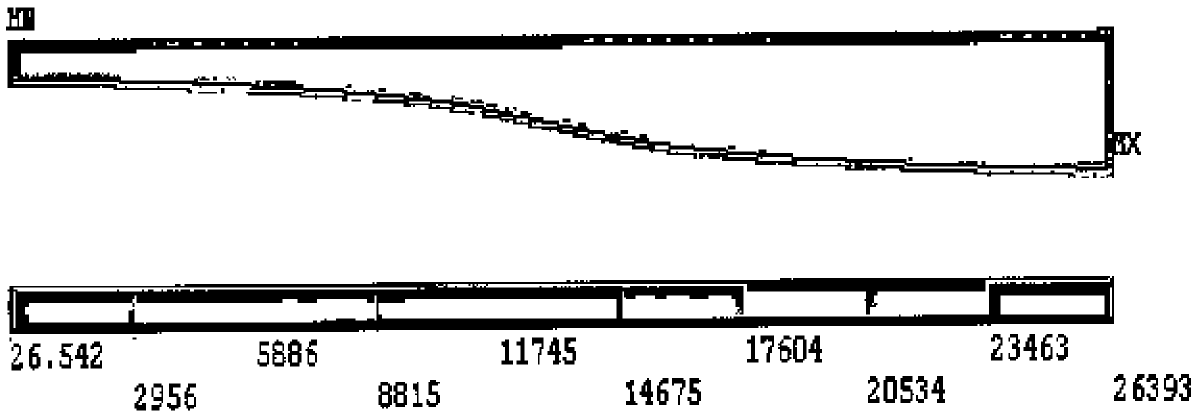

Figure 5.25. Plot of the first principal stresses for the RVE with CNT waviness ratio of (a/λ = 0.015) for perfect bonding under axial stretch (ΔL = 1 nm).

The finite element mesh of one of the long RVEs with 3 nm amplitude of sinusoidal CNT for imperfect bonding is shown in Fig. 5.26.

Figure 5.26: Partial view of the finite element mesh with 3 nm amplitude of sinusoidal CNT for imperfect bonding.

Now, the stress contour plot of the first principal stresses in the RVE with 3 nm amplitude of sinusoidal CNT for imperfect bonding, under axial stretch is shown in Fig. 5.27.

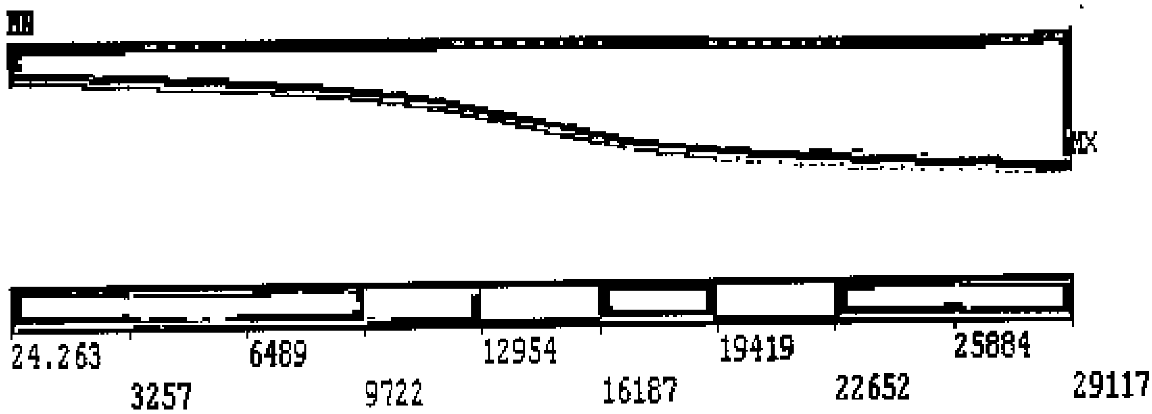

Figure 5.27: Plot of the first principal stresses for the RVE with CNT waviness ratio of ($a/\lambda = 0.015$) for imperfect bonding under axial stretch ($\Delta L = 1$ nm).

The FEM results for the CNT waviness ratio variation on the effective TEM of CNT-based composite with perfect and imperfect bonding studied is shown in Fig. 5.28. For imperfect bonding, both stiff and soft interphases between CNT and matrix are considered.

It is observed from Fig 5.28 that waviness ratio variation has a great impact on the effective TEM of nanocomposite. It is seen that effective TEM is strongly dependent on the waviness and rapidly decreases with increasing nanotube curvature. It also shows that stiff interphase has the same effect as perfect bonding with a higher value of TEM at a particular waviness ratio, while the soft interphase has lower value at that particular waviness ratio with the same effect. It suggests that it should be given great emphasize to reduce the waviness ratio of CNTs in the fabrication of CNT-based polymer composite when the higher Young's modulus is expected

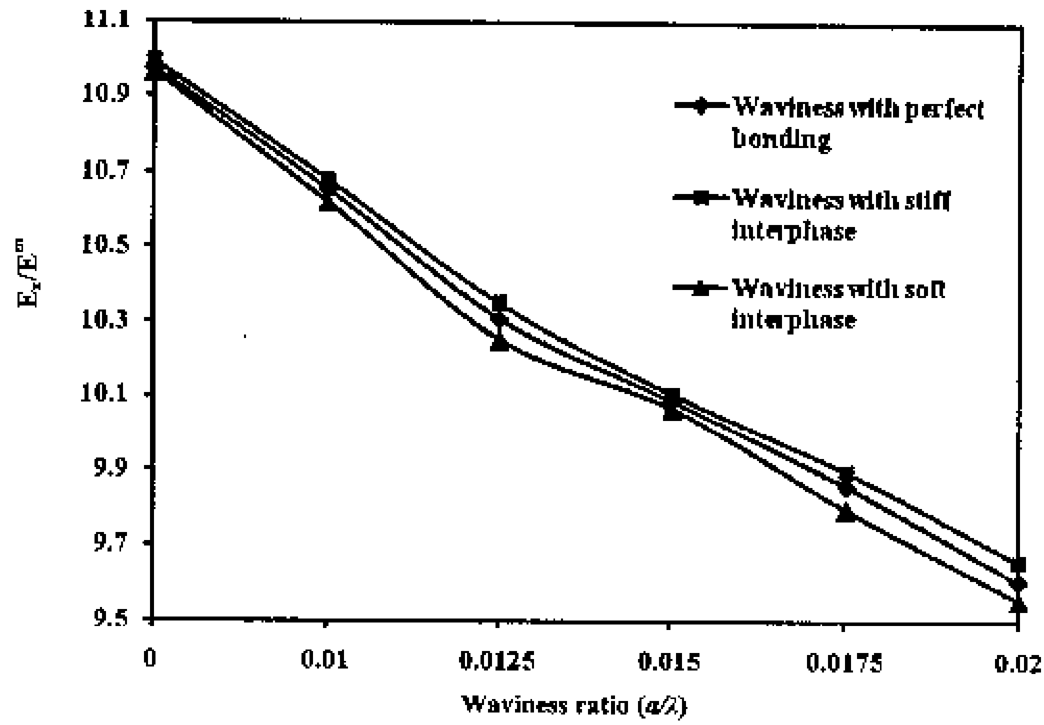

Figure 5.28: Effect of waviness ratio (a/λ) variation on the TEM of nanocomposite for wavelength ratio, λ/d = 13.406 (V_{CNT} = 5%).

5.6 EFFECT OF CNT WAVELENGTH ON THE TEM OF NANOCOMPOSITE

In this section, the effect of wavelength ratio (λ/d) on the effective TEM of nanocomposite for different values of waviness ratio (a/λ) is investigated. The investigation is carried out only for perfect bonding between CNT and matrix. The wavelength (λ) of the CNTs is considered same as in section 5.5. The amplitudes (a) are taken as 2, 3 and 4 nm to vary the waviness ratios (a/λ). The diameters (d) of CNTs are considered with indices of (65, 65), (80, 80), (95, 95) and (110, 110) to vary the wavelength ratios (λ/d). The Young's moduli and Poisson's ratios are considered same as considered in section 5.1.

The finite element mesh of one of the long RVEs with 4 nm amplitude of sinusoidal CNT is shown in Fig. 5.29

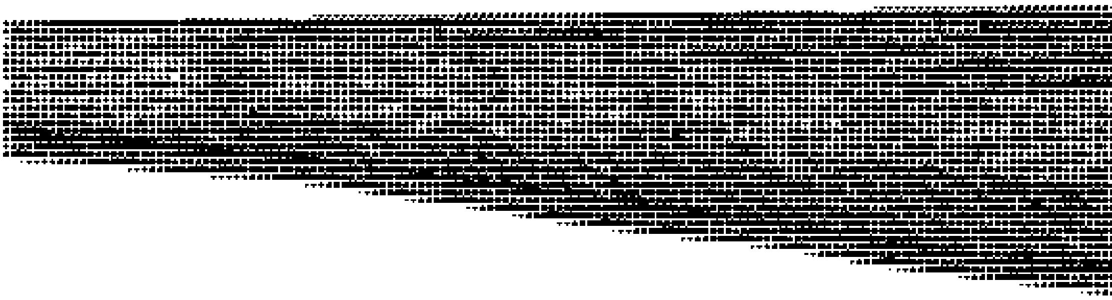

Figure 5 29: Partial view of the finite element mesh with 4 nm amplitude of sinusoidal CNT for perfect bonding.

The stress contour plot of the first principal stresses in the RVE with 4 nm of sinusoidal CNT amplitude, under axial stretch is shown in Fig. 5.30.

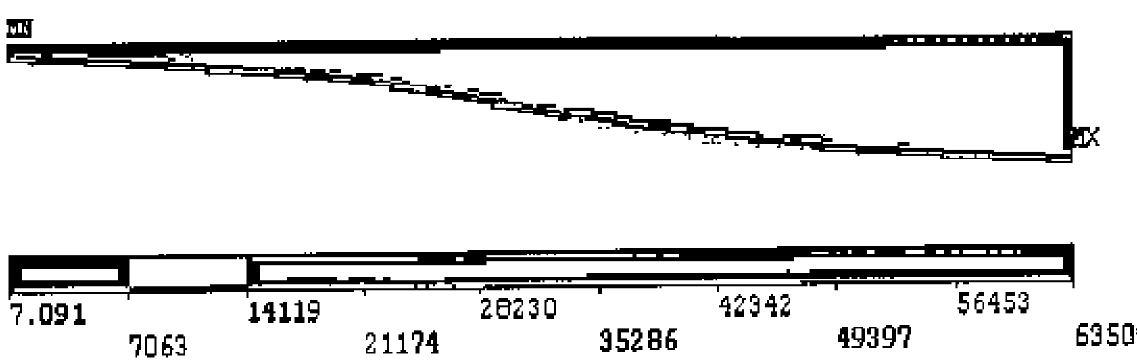

Figure 5.30: Plot of the first principal stresses for the RVE with CNT wavelength ratio of (λ/d = 13.406) under axial stretch (ΔL = 1 nm).

The FEM results for the CNT wavelength ratio (λ/d) variation for different values of waviness ratios on the effective TEM of CNT-based composite with perfect bonding studied is shown in Fig. 5.31.

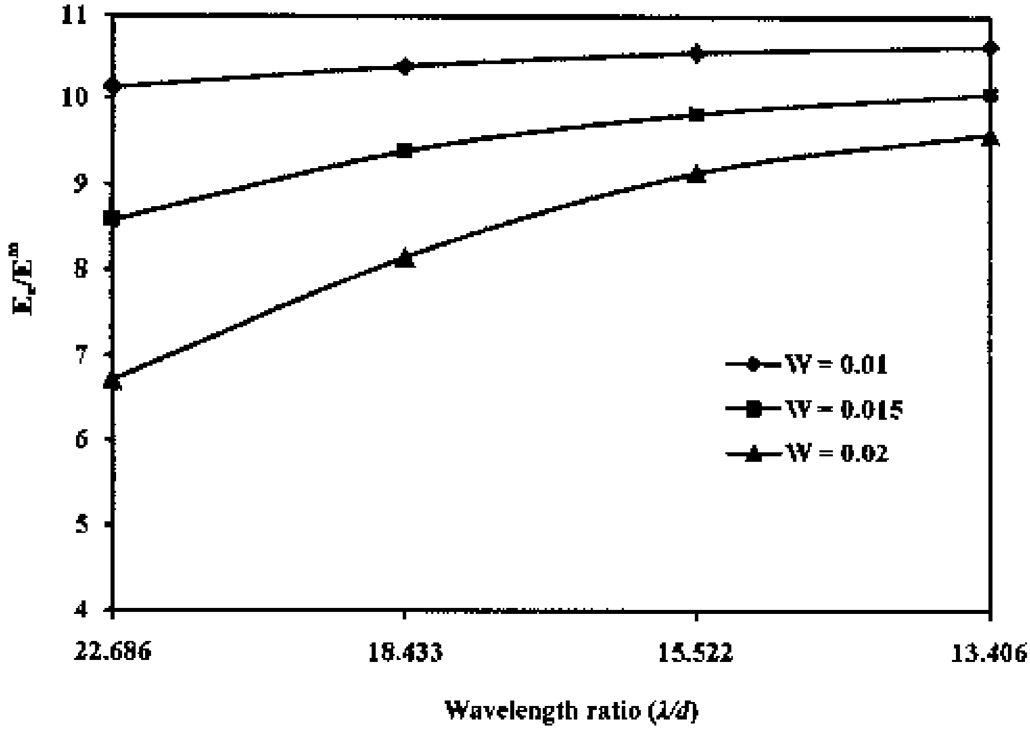

Figure 5.31: Effect of wavelength ratio (λ/d) variation on the TEM of nanocomposite for different values of waviness ratio (V_{CNT} = 5%).

Figure 5.31 shows the dependence of effective TEM on the wavelength ratio of the nanotube for different values of waviness ratio. It shows that for decreasing wavelength ratios the value of effective TEM converges to a constant valne (dependent on the waviness). Note that the critical wavelength ratio at which effective TEM can be considered to have reached a maximum is dependent on the waviness ratio. It means that for a given value of waviness ratio nanotubes with smaller wavelength ratio act stiffer.

CHAPTER 6
CONCLUSIONS AND RECOMMENDATIONS

Polymer systems reinforced with carbon nanotubes offer potential benefits over traditional reinforcement methods in terms of mechanical behavior. The degree of improvement for mechanical stiffness (Young's modulus) is dictated by a variety of factors, including nanotube diameter, size, bonding between the nanotube and the matrix, nanotube waviness and wavelength ratio effect in the matrix. The effective tensile elastic modulus (TEM) of carbon nanotube-based polymer composites has been investigated under these above mentioned conditions (or issues) of CNTs embedded in the polymer matrix using finite element method and the results are compared with the analytical results. In this chapter, the summary of the present work with important conclusions have been stated. Also some recommendations have been passed forward for further works.

6.1 CONCLUSIONS

The conclusions that can be summarized are presented below:

- For long CNT-based polymer composite, effective tensile elastic modulus increases with the increase in tube diameter for both perfect and imperfect bonding between CNT and matrix.

- For short CNT-based composite, effective tensile elastic modulus decreases with the increase in nanotube diameter for both perfect and imperfect bonding.
- In comparison to short CNT-based composite, effective tensile elastic modulus of long CNT-based composite is significantly higher for the same volume fraction of nanotube.
- Composite modulus increases with the increase in interphase thickness for stiff interphase whereas for soft interphase composite modulus decreases with the increase of interphase thickness.
- Effective tensile elastic modulus of nanocomposite increases with the increase in CNT wall thickness for long CNT.
- For short CNT-based polymer composite, effective tensile elastic modulus decreases with the increase in CNT wall thickness.
- Nanotube waviness significantly influences the effective tensile elastic modulus of nanocomposite and it decreases with the increase of waviness.
- Effective tensile elastic modulus of nanocomposite increases with the decrease in wavelength ratio for a certain value of nanotube waviness ratio.
- The rate of increment in effective modulus is higher for larger values of waviness ratio compared to the smaller values.

6.2 RECOMMENDATIONS

Many research issues need to be addressed in the modeling and simulations of CNTs in a matrix material for the development of nanocomposites. The present research work considered the RVEs as cylindrical in shape. Different type of RVEs, such as square and hexagonal, should be investigated. Again, different load cases and different solution methods should also be investigated. Analytical methods and simulation models to extract the mechanical properties of the CNT-based nanocomposites need to be further developed and verified with experimental results. While the procedure here is demonstrated using effective TEM calculations based on finite element results, alternative means to determine the appropriate value of TEM, incorporating more detailed information on the atomic level interactions in the material, could also be used in a similar analysis. Adaptations of the current model to include transversely isotropic nanotube behavior, inter-layer (MWNTs) and inter-tube (CNT bundles) sliding, finite end effects and exact nature of imperfect bonding between the nanotubes and the polymer, were not addressed here and warrant further work. Nanoscale interface cracks can be analyzed using simulations to investigate the failure mechanism in nanomaterials. Finally, large multiscale simulation models for CNT-based composites, which can link the models at the nano, micro and macro scales, need to be developed, with the help of molecular simulation, analytical and experimental work.

REFERENCES:

[1] Oberlin, A., Endo, M., and Koyama, T., "Filamentous growth of carbon through benzene decomposition", Journal of Crystal Growth, Vol-32, pp 335-349, 1976.

[2] Iijima, S., "Helical Microtubules Graphite Carbon", Nature, Vol-354, pp 56-58, 1991.

[3] Dresselhaus, M.S., Dresselhaus, G. and Saito, R., "Physics of carbon nanotubes", Carbon, Vol-37(7), pp 883–891, 1995.

[4] Bai, J.B. and Allaoui, A., "Effect of the length and the aggregate size of MWNTs on the improvement efficiency of the mechanical and electrical properties of nanocomposites – experimental investigation", Composites: Part A, Vol-34, pp 689-694, 2003.

[5] Treacy, M. M., Ebbesen, T. W., and Gibson, J. M., Nature, Vol-381, p 678, 1996.

[6] Wong, E.W., Sheehan, P. E., and Lieber, C. M., "Nanobeam mechanics: Elasticity, strength, and toughness of nanorods and nanotubes", Science, Vol-277, pp 1971-1975, 1997.

[7] Zhang, P., Huang, Y., Geubelle, P. H., Klein, P. A. and Hwang, K. C., International Journal of Solids and Structures, Vol-39, p 3893, 2002.

[8] Peebles, L. H., "Carbon Fibers: Formation, Structure and Properties", CRC Press, Boca Raton, 1995.

[9] Baughman, R.H., Zakhadov, A.A., and de Heer, W.A., "Carbon Nanotubes - the route toward applications", Science, Vol- 297, pp 787-792, 2002.

[10] Thostenson, E.T., Ren, Z. and Chou, T.W., "Advances in the science and technology of carbon nanotubes and their composites: a review", Composites Science and Technology, Vol- 61, pp 1899–1912, 2001.

[11] Collins, P.G. and Avouris, P., "Nanotubes for electronics", Scientific American, Vol- 283 (6), pp 67–69, 2000.

[12] Mintmire, J.W., Dunlap, B.I. and White, C.T., "Are fullerene tubules metallic?", Physics Review Letters, Vol- 68, pp 631–634, 1992.

[13] Tanaka, K., Okahara, K., Okada, M. and Yamabe, T., "Electronic properties of bucky-tube model", Chemical Physics Letters, Vol-191, pp 469-472, 1992.

[14] Hamada, N., Sawada, S. and Oshiyama, A., "New one-dimensional conductors: Graphitic microtubules", Physical Review Letters, Vol-68, pp 1579–1581, 1992.

[15] Iijima, S., Brabec, Ch., Maiti, A. and Bernholc, J., "Structural flexibility of carbon nanotubes", Journal of Physical Chemistry, Vol-104, pp 2089–2092, 1996.

[16] Qian, D., Dickey, E.C., Andrews, R. and Rantell, T., "Load transfer and deformation mechanisms in carbon nanotube-polystyrene composites", Applied Physics Letters, Vol-76 (20), pp 2868–2890, 2000.

[17] Allaoui, A., Bai, S., Cheng, H.M. and Bai, J.B., "Mechanical and electrical properties of MWNT/epoxy composite", Composite Science and Technology, Vol-62, pp 1993–1998, 2002.

[18] Wagner, H.D., Lourie, O., Feldman, Y. and Tenne, R., "Stress induced fragmentation of multiwall carbon nanotubes in a polymer matrix", Applied Physics Letters, Vol-72, pp 188– 190, 1998.

[19] Schadler, L.S., Giannaris, S.C., and Ajayan, P.M., "Load transfer in carbon nanotube epoxy composites", Applied Physics Letters, Vol-73, pp 3842–3844, 1998.

[20] Bower, C., Rosen, R., Jin, L., Han, J. and Zhou, O., "Deformation of carbon nanotubes in nanotube–polymer composites", Applied Physics Letters, Vol-74, pp 3317–3319, 1999.

[21] Liu, Y.J. and Chen, X.L., "Evaluations of the effective materials properties of carbon nanotube-based composites using a nanoscale representative volume element", Mechanics of Materials, Vol-35, pp 69–81, 2003.

[22] Jones, F.R., "Interphase formation and control in fibre composite materials", Key Engineering materials, Vol-116/117, pp 41-60, 1996.

[23] Smith, J.G., Watson, K.A., Thompson, C.M. and Connell, J.W., "Carbon nanotube/space durable polymer nanocomposite films for electrostatic charge dissipation", NASA Langley Research Center, Hampton, VA, ICASE Report No. 2002-2034, 2002.

[24] Parl, C., Ounaies, Z., Watson, K.A., Pawlowski, K., Lowther, S.E., Connell, J.W., Siochi, E.J., Harrison, J.S. and St. Clair, T.L., "Polymer-single wall carbon nanotube composites for potential spacecraft applications", NASA Langley Research Center, Hampton, VA, ICASE Report No. 2002-2036, 2002.

[25] Ci, L.J., Zhao, Z.G. and Bai, J.B., "Direct growth of carbon nanotubes on the surface of ceramic fibers", Carbon, Vol- 43, pp 855-894, 2005.

[26] Wang, X., Wang, X.Y. and Xiao, J., "A non-linear analysis of the bending modulus of carbon nanotubes with rippling deformation", Composite Structures, Vol-69, pp 315–321, 2005.

[27] Wang, X., Yang, H.K. and Yin, X.C., "Axially critical load of multiwall carbon nanotubes under thermal environment", Journal of Thermal Stresses, Vol-28 (2), pp 185-196, 2005.

[28] Zhang, Y.C. and Wang, X., "Thermal effects on interfacial stress transfer characteristics of carbon nanotubes/polymer composites", International Journal of Solids and Structures, Vol-42, pp 5399-5412, 2005.

[29] Sinnott, S.B., Shenderova, O.A., White, C.T., and Brenner, D.W., "Mechanical properties of nanotubule fibers and composites determined from theoretical calculations and simulations", Carbon, Vol-36, pp 1–9, 1998.

[30] Buongiorno Nardelli, M., Fattebert, J.L., Orlikowski, D., Roland, C., Zhao, Q. and Bernholc, J., "Mechanical properties, defects and electronic behavior of carbon nanotubes", Carbon, Vol-38, pp 1703–1711, 2000.

[31] Kang, J.W. and Hwang, H.J., "Mechanical deformation study of copper nanowire using atomistic simulation", Nanotechnology, Vol-12, pp 295–300, 2001.

[32] Griebel, M., and Hamaekers, J., "Molecular dynamics simulations of the elastic moduli of polymer carbon nanotube composites", Comput Meth Appl Mech Eng, Vol-193, pp 1773–1788, 2004.

[33] Sohlberg, K., Sumptor, B.G., Tuzun, R.E. and Noid, D.W., "Continuum methods of mechanics as a simplified approach to structural engineering of nanostructures", Nanotechnology, Vol-9, pp 30–36, 1998.

[34] Govindjee, S. and Sackman, J.L., "On the use of continuum mechanics to estimate the properties of nanotubes", Solid State Communications, Vol-110, pp 227–230, 1999.

[35] Ru, C.Q., "Column buckling of multiwalled carbon nanotubes with interlayer radial displacements", Physical Review B, Vol-62, pp 16962–16967, 2000.

[36] Ru, C.Q., "Axially compressed buckling of a doublewalled carbon nanotube embedded in an elastic medium", Journal of the Mechanics and Physics of Solids, Vol-49, pp 1265–1279, 2001.

[37] Das, P.S. and Wille, L.T., "Atomistic and continuum studies of carbon nanotubes under pressure", Computational Materials Science, Vol-24, pp 159–162, 2002.

[38] Qian, D., Liu, W.K. and Ruoff, R.S., "Mechanics of C_{60} in nanotubes", Journal of Physical Chemistry B, Vol-105, pp 10753–10758, 2001.

[39] Qian, D., Wagner, G.J., Liu, W.K. and Yu, M.F., et al., "Mechanics of carbon nanotubes", Applied Mechanics Reviews, Vol-55, pp 495–533, 2002.

[40] Qian, D., Liu, W.K. and Ruoff, R.S., "Load transfer mechanism in nanoropes", Composite Science and Technology, in press, 2003.

[41] Liu, Y.J. and Chen, X.L., "Continuum models of carbon nanotube-based composites by the BEM", Electronic Journal of Boundary Elements, in press, 2003.

[42] Liu, Y.J. and Chen, X.L., "Modeling and analysis of carbon nanotube-based composites using the FEM and BEM", Submitted to CMES: Computer Modeling in Engineering and Science, 2002.

[43] Hyer, M.W., "Stress Analysis of Fiber-Reinforced Composite Materials", McGraw-Hill, Boston, 1998.

[44] Nemat-Nasser, S. and Hori, M., "Micromechanics: Overall Properties of Heterogeneous Materials", Elsevier, Amsterdam, 1999.

[45] Chen, X.L., and Liu, Y.J., "Square representative volume elements for evaluating the effective material properties of carbon nanotube-based composites", Computational Materials Science, Vol-29, pp 1–11, 2004.

[46] Zeinkiewicz, O. C., "The finite element method", Third edition, Tata McGraw-Hill Publishing Company Limited, New Delhi, 1977.

[47] Stolarski, T. A., Nakasone, Y. and Yoshimoto, S., "Engineering analysis with ANSYS software", Elsevier Butterworth-Heinemann Publications Limited, 2006.

[48] Hutton, D. V., "Fundamentals of finite element analysis", McGraw-Hill Companies, Inc., 2004.

[49] Hayes, S. A., Lane, R., and Jones, F. R., "Fibre/Matrix stress transfer through a discrete interphase. Part 1: single-fibre model composites" Composites: Part A, Vol-32, pp 379-389, 2001.

[50] Munz, M., Strum, H., Sculz, E. and Hinrichsen, G., "The scanning force microscope as a tool for the detection of local mechanical properties within the interphase of fiber reinforced polymers", Composites: Part-A, Vol-29, pp 1251-1259, 1998.

[51] Mai, K., Maider, E., and Muhle, M., "Interphase characterisation in composites, with new non-destructive methods", Composites: Part-A, Vol-29, pp 1111-1119, 1998.

[52] Landingham, M. R., Dagastine, R. R., Eduljee, R. F., McCullogh, R. L., and Gillespie, J. W., "Characterisation of nanoscale property variations in polymer composite systems: 1. experimental results", Composites: Part- A, Vol-90, pp 75-83, 1999.

[53] Lopattananon, N., Kettle, A. P., Tripathi, D., Beck, A. J., Duval, F., France, R. M., Short, R. D. and Jones, F. R., "Interpface molecular engineering of carbon-fibre composites", Composites: Part-A, Vol-30, pp 49-57, 1999.

[54] Xin, Z., Jianjun, Z. and Zhong-can, O-Y., "Strain energy and Young's modulus of single-wall carbon nanotubes calculated from electronic energy-band theory", Physical Review B, Vol-62, p 13692, 2000.

[55] Jin, L., Bower, C. and Zhou, O., "Alignment of carbon nanotubes in a polymer matrix by mechanical stretching", Applied Physics Letters, Vol-73, p 1197, 1198.

[56] Fisher, F. T., Bradshaw, R. D. and Brinson, L. C., "Fiber waviness in nanotube-reinforced polymer composites—1: modulus predictions using effective nanotube properties", Composites Science and Technology, Vol-63, pp 1689-1703, 2003.

[57] Shaffer, M. S. P. and Windle, A. H., "Fabrication and characterization of carbon nanotube/poly (vinyl alcohl) composites", Advanced Materials, Vol-11, p 937, 1999.